

1 **Improving the constraint on the M_w 7.1 2016 off-Fukushima shallow normal-**
2 **faulting earthquake with the high azimuthal coverage tsunami data from the**
3 **S-net wide and dense network: Implication for the stress regime in the**
4 **Tohoku overriding plate**

5
6 **Tatsuya Kubota¹, Hisahiko Kubo¹, Keisuke Yoshida², Naotaka Y. Chikasada¹, Wataru**
7 **Suzuki¹, Takeshi Nakamura³, and Hiroaki Tsushima⁴**

8
9 ¹ National Research Institute for Earth Science and Disaster Resilience, Tsukuba, Japan.

10 ² Graduate School of Science, Tohoku University, Sendai, Japan.

11 ³ Central Research Institute of Electric Power Industry, Abiko, Japan.

12 ⁴ Meteorological Research Institute, Japan Meteorological Agency, Tsukuba, Japan

13
14 Corresponding author: Tatsuya Kubota (kubotatsu@bosai.go.jp)

15
16 **Key Points:**

- 17 • Tsunamis due to the 2016 off-Fukushima shallow normal-faulting earthquake were
18 observed by the S-net wide and dense pressure gauge network
- 19 • Use of the near-field and the high-coverage array significantly improved the constraint of
20 the fault modeling of the 2016 earthquake
- 21 • Our fault model suggested that the stress around the focal area should be in a normal-
22 faulting regime even before the 2011 Tohoku earthquake

23

24 Abstract

25 Tsunamis with maximum amplitudes of up to 40 cm, related to the M_w 7.1 normal-
26 faulting earthquake off Fukushima, Japan, on November 21, 2016 (UTC), were clearly recorded
27 by a new offshore wide and dense ocean bottom pressure gauge network, S-net, with high
28 azimuthal coverage located closer to the focal area. We processed the S-net data and found that
29 some stations included the tsunami-irrelevant drift and step signals. We then analyzed the S-net
30 data to infer the tsunami source distribution. A subsidence region with a narrow spatial extent
31 (~ 40 km) and a large peak (~ 200 cm) was obtained. The other near-coastal waveforms not used
32 for the inversion analysis were also reproduced very well. Our fault model suggests that the
33 stress drop of this earthquake is ~ 10 MPa, whereas the shear stress increase along the fault
34 caused by the 2011 Tohoku earthquake was only ~ 2 MPa. Past studies have suggested that
35 horizontal compressional stress around this region switched to horizontal extensional stress after
36 the Tohoku earthquake due to the stress change. The present result, however, suggests that the
37 horizontal extensional stress was locally predominant at the shallowest surface around this region
38 even before the 2011 Tohoku earthquake. The present study demonstrates that the S-net high-
39 azimuthal-coverage pressure data provides a significant constraint on the fault modeling, which
40 enables us to discuss the stress regime within the overriding plate around the offshore region.
41 Our analysis provides an implication for the crustal stress state, which is important for
42 understanding the generation mechanisms of the intraplate earthquake.

43

44 Plain Language Summary

45 On November 21, 2016 (UTC), a large earthquake occurred within the continental plate
46 off Fukushima, Japan, and a new seafloor tsunami network, S-net, recorded its tsunamis with
47 much higher azimuthal coverage and with shorter epicentral distance than any of the previous
48 networks. We analyzed the S-net data to reveal the rupture process of this earthquake. Our result
49 explained all of the S-net data and the other tsunami network data very well. According to past
50 studies, the continental plate in northeastern Japan was under horizontal compression before the
51 2011 Tohoku earthquake due to the pushing force by the subducting oceanic plate. However, our
52 rupture modeling result suggested that the plate around the earthquake rupture area was
53 horizontally stretched even before the Tohoku earthquake, so that the off-Fukushima earthquake
54 occurred. Our study demonstrated that the S-net, which has high spatial coverage, makes it

55 possible to reveal the rupture model of offshore earthquakes, which was difficult in the past
56 before S-net became available. The S-net will also enable us to discuss the impact of the Tohoku
57 earthquake on the crustal stress, which is necessary for understanding the earthquake generation
58 mechanics.

59

60 **1 Introduction**

61 In this decade, the coseismic rupture process of the 2011 Tohoku earthquake and its
62 preseismic and postseismic processes have been investigated in detail (e.g., Hino, 2015; Kodaira
63 et al., 2020; 2021; Lay, 2018; Uchida & Burgmann, 2021; Wang et al., 2018). In response to the
64 Tohoku earthquake, a new wide offshore deep-ocean observation network, Seafloor Observation
65 Network for Earthquakes and Tsunamis along the Japan Trench (S-net), has been constructed off
66 eastern Japan (Aoi et al., 2020; Kanazawa et al., 2016; Mochizuki et al., 2017; Uehira et al.,
67 2016, Figure 1a). Recent studies have started to utilize S-net ocean bottom seismometers to
68 investigate the seismotectonics and geodynamics in the Tohoku subduction zone (Hua et al.,
69 2020; Matsubara et al., 2019; Nishikawa et al., 2019; Sawazaki & Nakamura, 2020; Takagi et al.,
70 2019, 2021; Tanaka et al., 2019; Uchida et al., 2020; Yu & Zhao, 2020). The S-net also
71 incorporates ocean-bottom pressure gauges (OBPGs), which are expected to be utilized for
72 tsunami forecasts (e.g., Aoi et al., 2019; Inoue et al., 2019; Mulia & Satake, 2021; Tanioka,
73 2020; Tsushima & Yamamoto, 2020; Wang et al., 2021; Yamamoto Aoi et al., 2016; Yamamoto,
74 Hirata et al., 2016). The other potential contributions to the earth sciences of the S-net OBPG
75 have also been demonstrated, such as understanding the wave propagation process in the ocean
76 as well as the rupture process of subseafloor earthquakes (Kubota, Saito, & Suzuki, 2020;
77 Kubota et al., 2021; Saito & Kubota, 2020; Saito et al., 2021). The wide and dense network data
78 of S-net will significantly broaden our understanding of the Tohoku subduction zone after the
79 Tohoku earthquake.

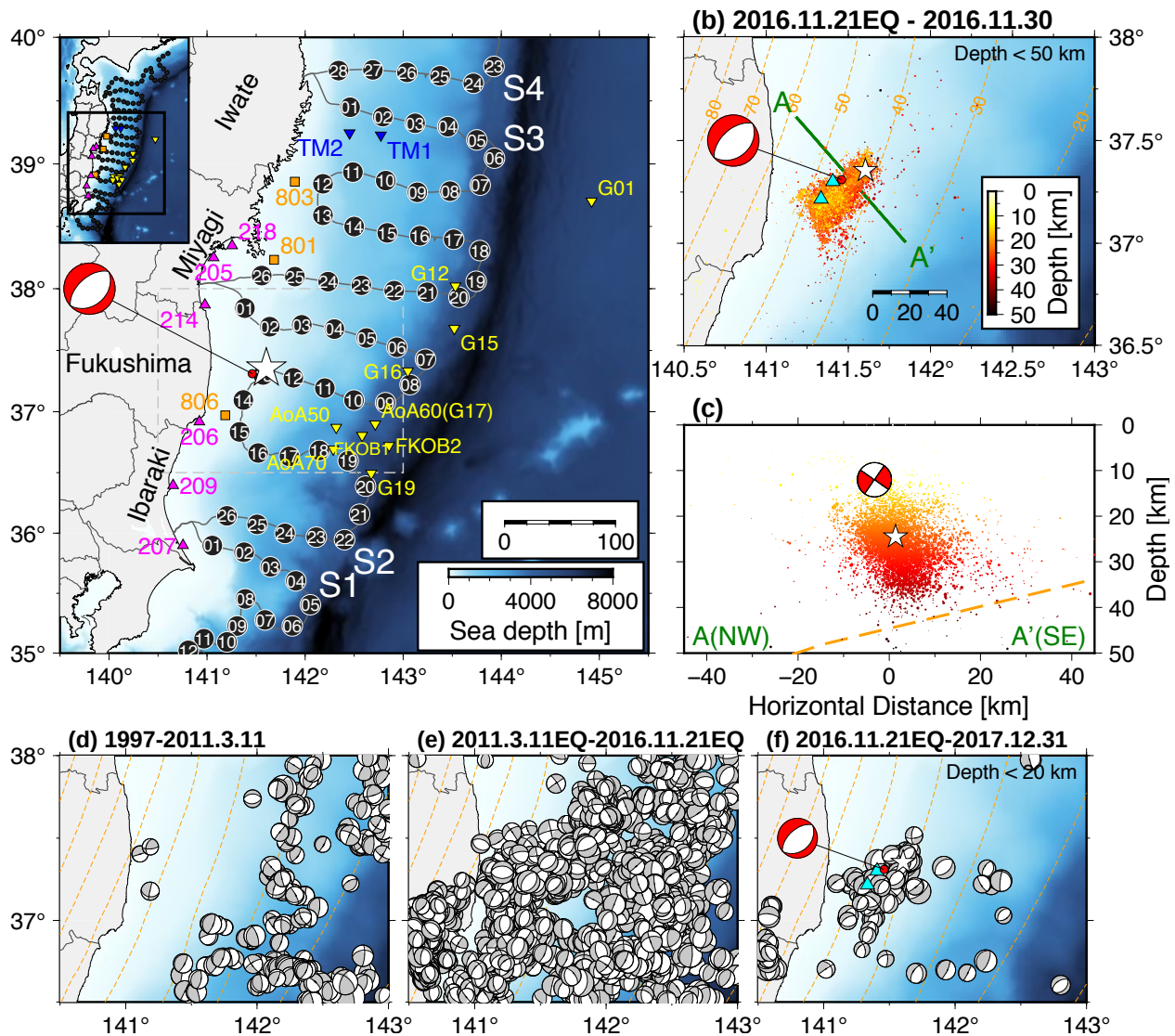
80 On November 21, 2016, a major shallow normal-faulting earthquake occurred within
81 the overriding plate off Fukushima Prefecture (20:59 UTC, M_w 6.9, 12 km, Global CMT
82 [GCMT], <https://www.globalcmt.org>, Figure 1, hereafter referred to as the off-Fukushima
83 earthquake). Compared with the GCMT centroid, its epicenter, as determined by Japan
84 Meteorological Agency (JMA), was located ~20 km east to northeast (white star in Figure 1).
85 Numerous aftershocks accompanied this earthquake (Figures 1b and 1c). It has been reported
86 that the tsunamis associated with the off-Fukushima earthquake were observed by onshore and
87 offshore tsunami networks (e.g., Gusman et al., 2017; Kawaguchi et al., 2017; Suppasri et al.,
88 2017). However, these stations were located only on the shore-side from the focal area, and the
89 source-station distances are large (Figure 1a). In contrast, the S-net OBPGs recorded tsunamis
90 with much higher azimuthal coverage and with a closer distance to the focal area (~30 km,

91 Figure 1a). Because of the much better station coverage of the S-net, the constraint on the initial
92 sea height (tsunami source) estimation and the finite fault modeling of the off-Fukushima
93 earthquake will be significantly increased, as compared with the previous datasets.

94 The normal-faulting mechanism of the off-Fukushima earthquake is similar to nearby
95 shallow normal-faulting micro-seismicity within the overriding plate, with a tensile axis (σ_3)
96 oriented in basically the east-west direction, which significantly increased after the Tohoku
97 earthquake (Figures 1d–1f, e.g., Asano et al., 2011; Hardebeck & Okada, 2018; Hasegawa et al.,
98 2012; Tanaka et al., 2014; Wang et al., 2019; Yoshida et al., 2012). This increase in the normal-
99 faulting seismicity is considered to be related to the significant stress perturbation by the Tohoku
100 earthquake, which switched the intraplate stress regime from horizontal compression to
101 horizontal extension (e.g., Hasegawa et al. 2012). If we can obtain a detailed fault model of the
102 off-Fukushima earthquake, then the quantitative relationship between the crustal stress released
103 during the off-Fukushima earthquake and the stress increase due to the 2011 Tohoku earthquake
104 can be discussed. This quantitative comparison will be useful to deepen our understanding of the
105 temporal change of the crustal stress state associated with the Tohoku earthquake.

106 In the present study, we therefore estimate the detailed finite fault model of the off-
107 Fukushima earthquake using the S-net OBPB data. From the finite fault model, we also attempt
108 to examine the normal-faulting stress state within the crust around the off-Fukushima earthquake
109 and its relationship with the Tohoku earthquake. The OBPB data process is described in Section
110 2, and Section 3 summarizes the feature in the S-net OBPB data. The spatial distribution of the
111 initial sea surface height (tsunami source) and the finite fault model of the off-Fukushima
112 earthquake are estimated in Sections 4 and 5, respectively. Section 6 examines the relationship
113 between the Tohoku earthquake and the stress regime around the focal area. Section 7 concludes
114 the present study.

115



116
 117 **Figure 1.** (a) Location map of the present study. Locations of the tsunami stations are shown by
 118 colored symbols (black circle: S-net OBPG, blue inverted triangle: ERI OBPG, yellow inverted
 119 triangle: Tohoku University OBPG, orange square: NOWPHAS GPS buoy, pink triangle:
 120 NOWPHAS wave gauge). The epicenter (white star) and the CMT solution (red) of the off-
 121 Fukushima earthquake are taken from JMA and GCMT, respectively. (b) Enlarged view of the
 122 rectangular area drawn by gray lines in Figure 1a. Aftershocks during about one week as
 123 determined by JMA are shown (color denotes its depth). Orange contours show the depth of the
 124 subducting plate interface (Nakajima & Hasegawa, 2006). The locations of fresh seafloor cracks
 125 found by the JAMSTEC survey are shown by blue triangles. (c) Vertical cross section along line
 126 A-A' in Figure 1b. (d–f) The F-net fault mechanisms (Fukuyama et al., 1998) at depths shallower

127 than 20 km, (d) before the Tohoku earthquake, (e) during the Tohoku earthquake and the off-
128 Fukushima earthquake, and (f) after the off-Fukushima earthquake.

129

130 **2 Tsunami dataset**

131 The present study used the S-net OBP data (black circles in Figure 1a), which was
132 also used by Wang & Satake (2021). Although S-net now consists of 150 observatories (Aoi et
133 al., 2020), 25 of these observatories, located at the outer-trench region, were not installed when
134 the off-Fukushima earthquake occurred. Each observatory is equipped with absolute pressure
135 sensors manufactured by Paroscientific, Inc. (e.g., Polster et al., 2009; Watts & Kontoyianiss,
136 1996). Two pressure sensors are equipped in each observatory for redundancy. The sensors are
137 not directly exposed to the seawater, but rather are sealed in a metal housing filled with oil. The
138 metal housing is further sealed in a metal cylindrical vessel filled with oil. The external pressure
139 is transferred to the pressure sensor inside via a diaphragm made of hard rubber. See Aoi et al.
140 (2020) for more details.

141 In addition to S-net, we use other OBPGs to evaluate the modeling resolution. We use
142 the OBPGs off Iwate Prefecture installed by the Earthquake Research Institute (ERI) of the
143 University of Tokyo (blue inverted triangles in Figure 1a, Gusman et al., 2017; Kanazawa &
144 Hasegawa, 1997) and the OBPGs off eastern Japan installed by Tohoku University (yellow
145 inverted triangles, Hino et al., 2014). We also use the offshore GPS buoys (orange squares) and
146 wave gauges (pink triangles) of the Nationwide Ocean Wave information network for Ports and
147 HARbourS [NOWPHAS] (Kawaguchi et al., 2017; Nagai et al., 1998).

148

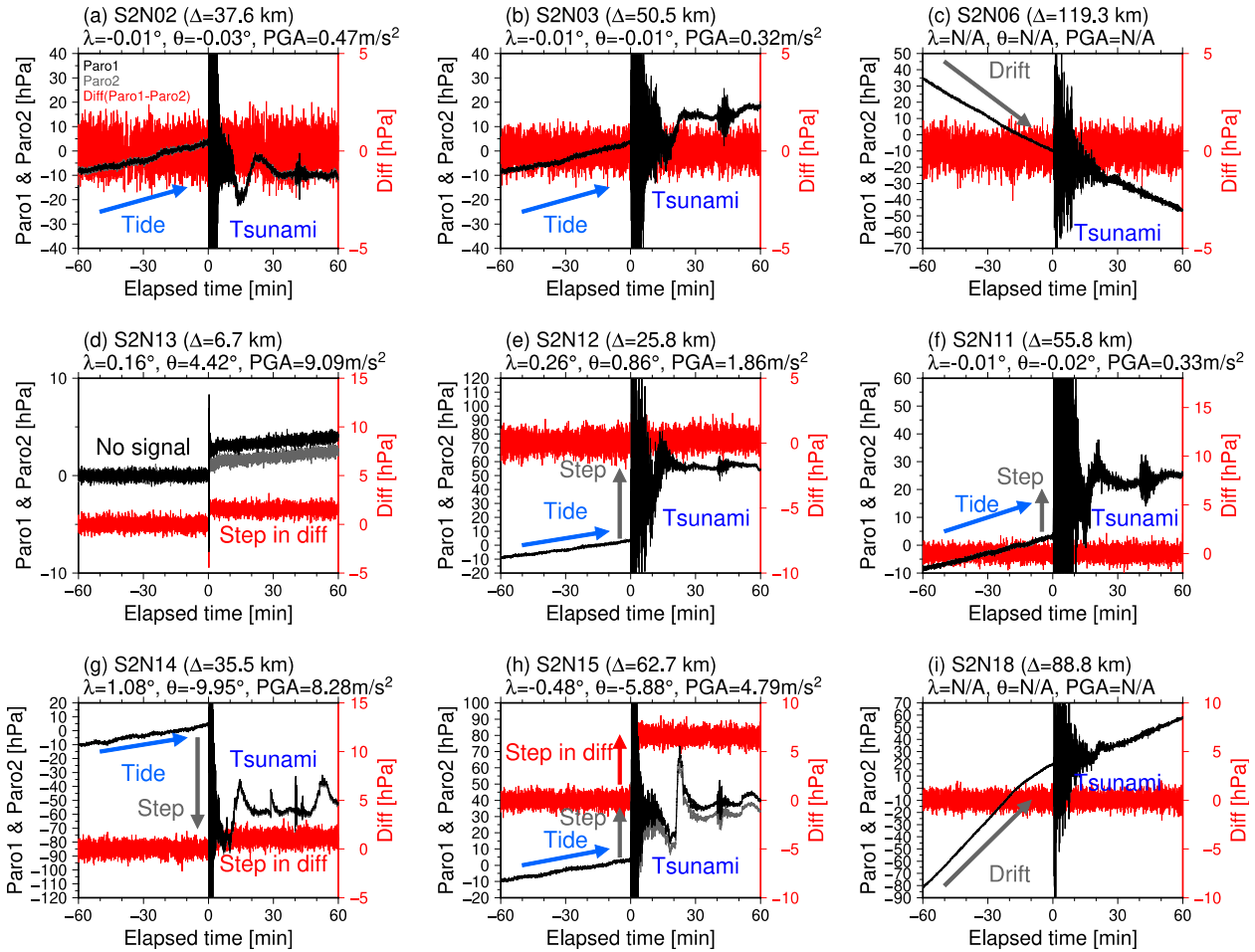
149 **3 Fundamental feature of the S-net OBPGs: Tsunami-irrelevant pressure signals**

150 In order to investigate the fundamental feature of the S-net OBP data signals, we first
151 process the OBP data. We decimate the original 10 Hz data to 1 Hz (Figure 2). We then
152 subtract the theoretical tide calculated by the model of Matsumoto et al. (2000) and apply a low-
153 pass filter with a cutoff of 100 s to reduce the high-frequency seismic wave signals (Figure 3).

154 Figure 2 shows the 1-Hz-sampling pressure waveforms. The high-frequency
155 fluctuations related to the seismic waves and ocean-acoustic waves (e.g., Kubota, Saito,
156 Chikasada et al., 2020) are observed. The gradual pressure increases related to the ocean tide are
157 also observed, although some traces show different trends. The pressure changes recorded by the

158 two sensors equipped in the same observatory (black and gray lines) are very similar to each
 159 other. The difference between these two traces (red lines) is around zero, although some stations
 160 have offsets in the differences. At station S2N13, which is located just above the focal area of the
 161 off-Fukushima earthquake, no seismic or tsunamis signals were recorded.

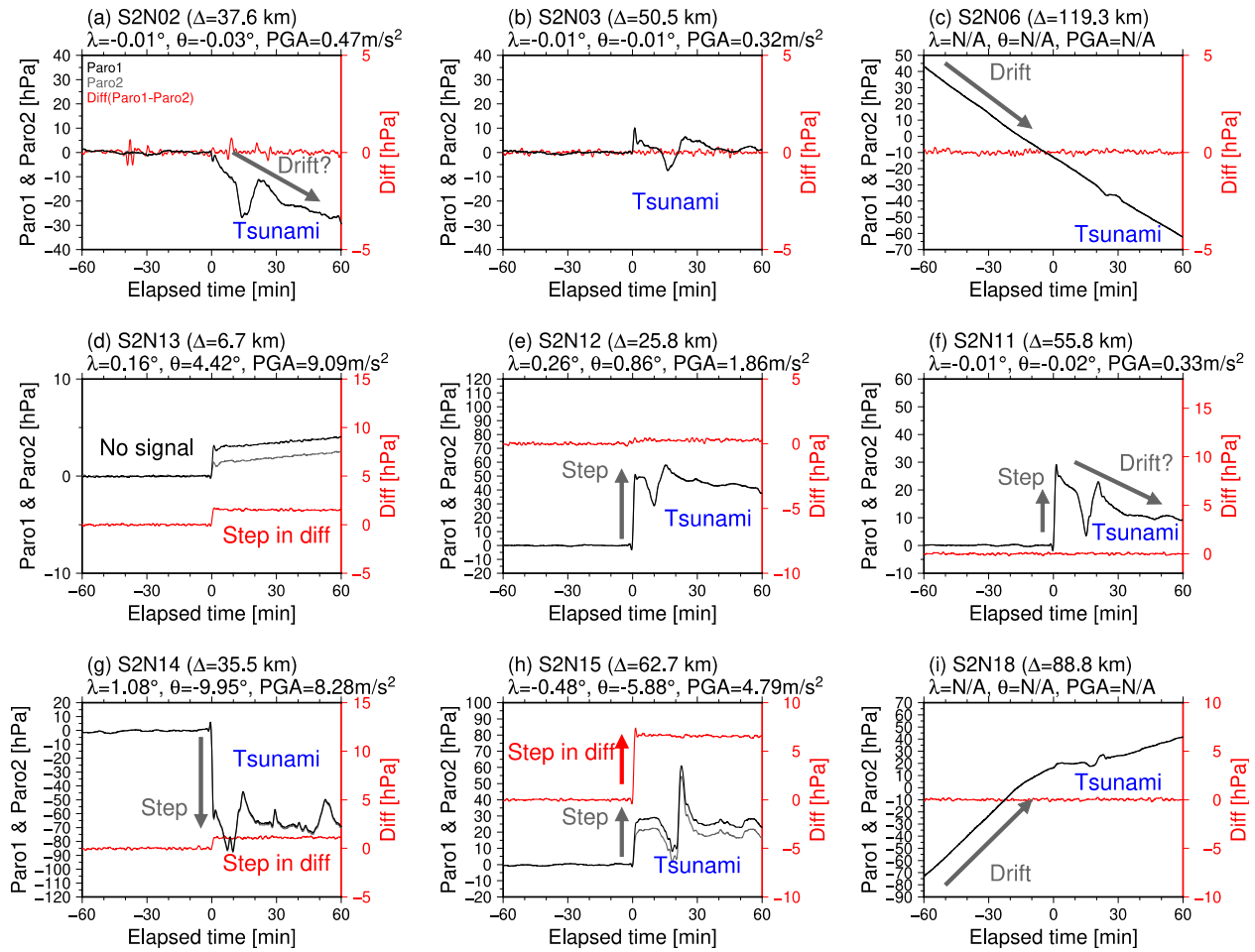
162



163

164 **Figure 2.** The 1-Hz ocean-bottom pressure waveforms for stations (a) S2N02, (b) S2N03, (c)
 165 S2N06, (d) S2N13, (e) S2N12, (f) S2N11, (g) S2N14, (h) S2N15, and (i) S2N18. Black and gray
 166 traces denote the waveforms from each of the pressure sensors. Red traces denote the difference
 167 between the two sensors. Note that the vertical scale for the difference waveforms is different in
 168 each subfigure. The dominant signals are indicated by arrows and text. The epicentral distance Δ
 169 measured from the JMA epicenter, and the tilt change λ , rotation angle change θ , and PGA
 170 values measured by the co-equipped accelerometer (Takagi et al., 2019) are also shown.

171



172

173 **Figure 3.** Ocean-bottom pressure waveforms after data processing for the stations. See Figure 2

174 for a detailed description.

175

176 Although the tsunamis are confirmed in the lowpass-filtered S-net OBPG waveforms

177 (Figure 3), we also recognize some unfamiliar pressure signals irrelevant to the tsunamis, such as

178 the large drift components (e.g., S2N06, S2N18). Since the observed drift rates are very large

179 (e.g., ~ 50 hPa/hour at S2N06), these drifts are considered to be due to neither tsunamis nor

180 postseismic seafloor deformations. It might be possible that the mechanical drifts of the pressure

181 sensors are the cause of these drifts, because it was reported that the Paroscientific pressure

182 sensors contain instrumental drift with rates of ~ 8.8 hPa/year (Inazu & Hino, 2011; Polster et al.

183 2009; Watts & Kontoyianiss, 1996). However, the previously-reported drift rates of the

184 Paroscientific pressure sensors are much smaller than those confirmed in the S-net. In addition, it

185 is incomprehensible that the drift rates are completely identical in the sensor pair, although the

186 drift rates must be different in each sensor. Therefore, we do not consider the cause of these

187 drifts to be as previously reported. Although we cannot identify the reason for these drifts, we
188 suspect the observation system of the S-net may be related to the cause of the drift.

189 In addition, abrupt steps at the origin time are observed at some OBPGs, particularly at
190 S2N11, S2N12, S2N14, and S2N15. The step is also observed at S2N13, where no tsunami
191 signals were recorded (Figure 3d). If we consider the pressure offset changes as a result of the
192 seafloor vertical movement, these pressure changes correspond to a seafloor vertical
193 displacement of ~30–60 cm (assuming a pressure change of 1 hPa is equal to a seawater column
194 height change of 1 cm H₂O). Considering the source-station distances, these displacements seem
195 too large compared with those expected from typical M~7 earthquakes. Furthermore, even if the
196 OBPGs are located inside the focal area where the vertical displacement is large, the ocean-
197 bottom pressure, or the seawater column height above the OBPG, cannot change so abruptly
198 because both seafloor and sea-surface simultaneously move vertically during tsunami generation
199 (e.g., Tsushima et al. 2012). Therefore, these steps are unlikely to be caused by the seafloor
200 permanent displacement. Similar pressure steps were also recorded by the S-net and the other
201 OBPG networks during the past earthquakes (Kubota, Suzuki et al., 2018; Kubota, Saito, Suzuki,
202 2020; Wallace et al. 2016), which are not considered to be related to the tsunami or the seafloor
203 crustal deformation.

204 It has been reported that outputs of Paroscientific pressure sensors strongly depend on
205 its orientation relative to the direction of gravity (Chadwick et al., 2006). Thus, the step signals
206 might be caused by the rotation of the pressure sensor. According to Chadwick et al. (2006), the
207 rotation angle change of the pressure sensor of $\theta \sim 10^\circ$ roughly corresponds to the apparent
208 pressure offset change of up to ~10 hPa. Takagi et al. (2019) analyzed the co-equipped
209 accelerometer during the off-Fukushima earthquake and found that some observatories near the
210 epicenter rotated associated with large seafloor ground motion (Figures 2 and 3). However,
211 comparing the rotation angles at some near-source stations (e.g., $\theta = 0.86^\circ$ at S2N12 and 9.95° at
212 S2N14, Takagi et al., 2019), the observed pressure steps were extremely large ($> \sim 50$ hPa).
213 Furthermore, considering that the sensitivity to the rotation angle must be different in each
214 sensor, it is quite strange that the amounts of the pressure step in two pressure sensors are almost
215 identical. We also confirm that the pressure steps in the two pressure sensors are different at
216 some stations where the large rotation was observed (e.g., S2N13, S2N15), leading to the steps
217 around the focal time in the difference traces between the two sensor outputs (red lines in Figure

218 3). Taking these points into account, we consider that the dominant cause of the pressure steps is
219 not the response to the sensor rotation, as reported by Chadwick et al. (2006), but might be the
220 observation system of the S-net, and the difference in the steps between the two sensors may be
221 due to the difference in the response to the rotation angle. As a summary of this section, we
222 emphasize that we must be careful to analyze the OBPG data to distinguish whether such signals
223 are real or are artifacts related to the drift or offset, although the S-net OBPGs clearly recorded
224 the tsunamis due to the 2016 off-Fukushima earthquake.

225

226 **4 Tsunami source modeling**

227 4.1 Modeling procedure

228 In this section, we analyze the S-net data to estimate the spatial distribution of initial
229 sea-surface height (tsunami source) of the off-Fukushima earthquake and to investigate how the
230 S-net OBPGs provide better constraint. In order to reduce the long-period tsunami-irrelevant
231 drift signals as well as the short-period seismic wave components, we apply the bandpass filter
232 with passbands of 100–3,600 s (Figure 4b). We here briefly describe the procedure for the
233 tsunami source modeling. The full details are shown in Text S1.

234 We set the analytical area as 50 km × 50 km (rectangular area in Figure 4a) and
235 distribute the unit source elements of the seafloor vertical displacement with horizontal spatial
236 intervals of 2 km. Assuming that the seafloor displacement from the unit source elements is
237 equivalent to the initial sea-surface height change, we simulate a tsunami by solving a linear
238 dispersive tsunami equation (Saito, 2019; Saito et al., 2010). We use the JTOPO30 bathymetry
239 data with a spatial resolution of 30 arcsec (<http://www.mirc.jha.jp/en/>), interpolating the spatial
240 interval of $\Delta x = \Delta y = 1$ km. The displacement is assumed to occur instantaneously at time $t = 0$ s.
241 After calculation, the pressure offset change due to the seafloor displacement is subtracted from
242 the sea-surface height change assuming that a sea height change of 1 cm H₂O is equal to a
243 pressure change of 1 hPa (the method of Tsushima et al., 2012). We finally apply the same
244 bandpass filter to the simulated waveform as that applied to the observation.

245 In the inversion analysis, we use the time-derivative waveforms for the inversion
246 analysis ($\partial p / \partial t$, the method of Kubota, Suzuki et al. (2018)), because the time-derivative can
247 reduce the artificials due to the tsunami-irrelevant steps, which becomes the impulse and thus
248 does not contain the offset change. The data time window used for the modeling is manually

249 determined, which includes the main part of the tsunami (indicated by the blue traces in Figure
 250 4c). The goodness of the estimated source is evaluated using the variance reduction (VR):

251

$$252 \quad VR = \left(1 - \frac{\sum_i (d_i^{obs} - d_i^{cal})^2}{\sum_i d_i^{obs2}} \right) \times 100 (\%) \quad (1)$$

253

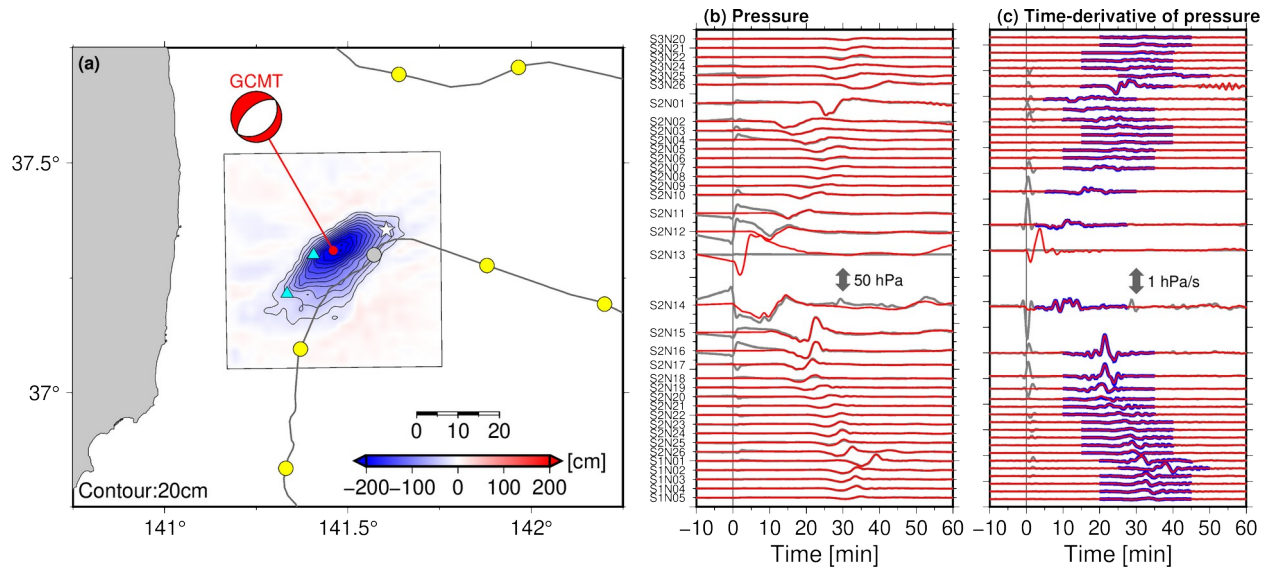
254 where d_i^{obs} and d_i^{cal} are the i -th data of the observed and calculated time-derivative pressure
 255 waveforms. We impose the smoothing constraint for the inversion, and its weight is determined
 256 based on the trade-off between the weight and the VR (Figure S1) to avoid both the overfitting
 257 and oversmoothing of data.

258

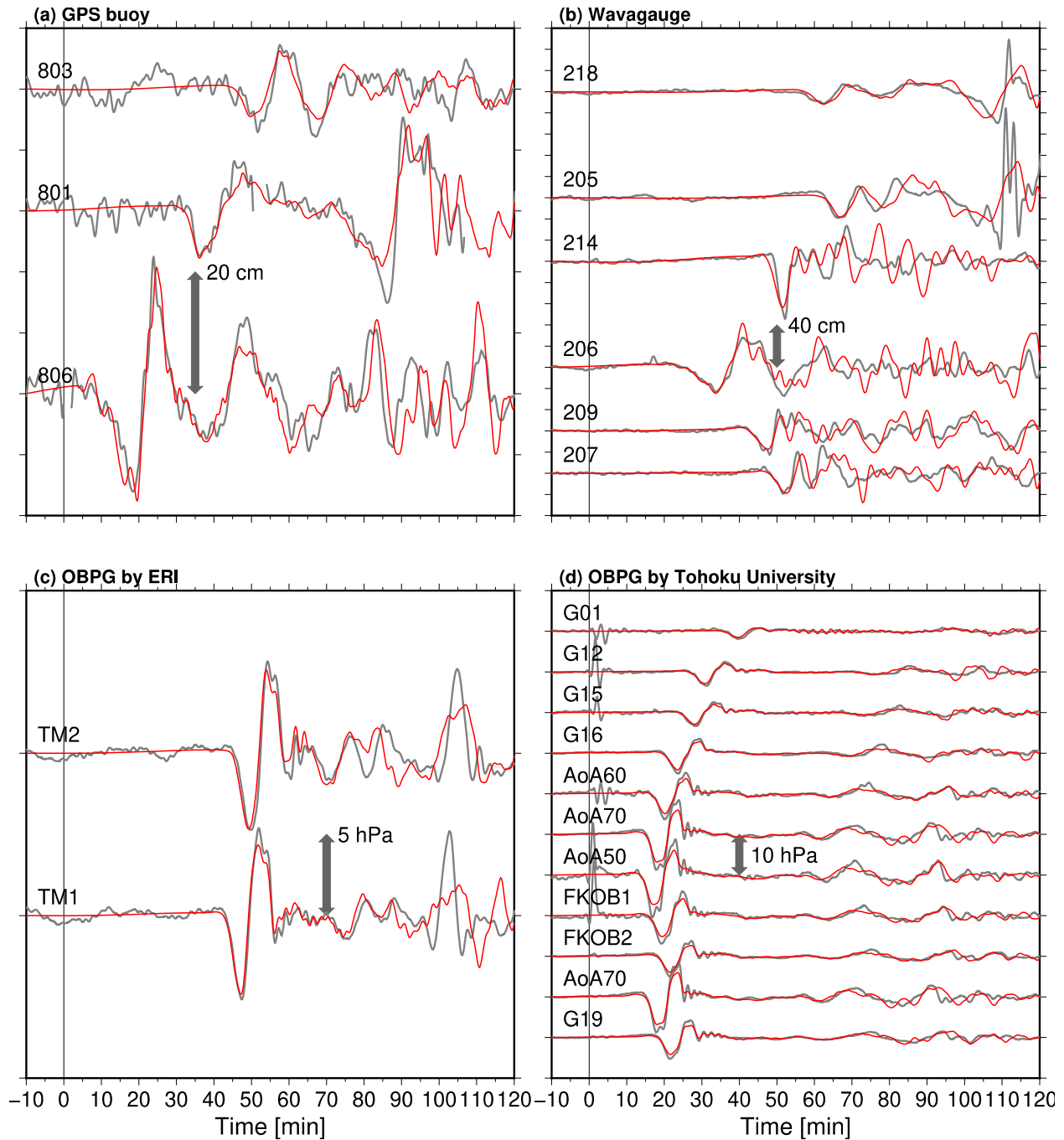
259 4.2 Results

260 Figure 4 shows the results of the inversion. A subsidence with a horizontal extent of
 261 $\sim 40 \text{ km} \times \sim 20 \text{ km}$, having a sharp peak near the GCMT centroid, was obtained (Figure 4a). The
 262 direction of the northeast-southwest extents of the subsided region is consistent with the GCMT
 263 strike angle of 49° . The northwest edge of the subsidence region is consistent with the locations
 264 where the seafloor displacements of 1–2 m and fresh seafloor cracks were found by a seafloor
 265 bathymetry survey just after the off-Fukushima earthquake conducted by Japan Agency for
 266 Marine-Earth Science and Technology [JAMSTEC] (blue triangles in Figure 4a). The time
 267 derivatives of the S-net pressure waveforms were well reproduced (VR = 95.7%, Figure 4c).
 268 Except for the waveforms just after the focal time at some near-source OBPGs, the observed
 269 pressure is also well explained (Figure 4b). The waveforms recorded at the other tsunami stations
 270 (Figure 1a) are also reproduced surprisingly well (Figure 5), even though they were not used for
 271 the inversion. This suggests that the use of the S-net tsunami data provides good spatial
 272 resolution of the tsunami source, and thus it is expected that we can obtain a reliable fault model.
 273 Note that the later arrivals in some stations (e.g., $\sim 100 \text{ min}$ at TM1 and TM2) are not well
 274 reproduced, which are caused by the coastal-reflections (Gusman et al., 2017). This is probably
 275 because the spatial resolution of the coastal shape from the topography data in our simulation is

276 not sufficient ($\Delta x = \Delta y = 1$ km) to reproduce the reflected tsunami waves, and the high-resolution
 277 bathymetry data is important to reproduce the reflected tsunamis (Gusman et al., 2017; Kubota,
 278 Saito et al., 2018).
 279



280
 281 **Figure 4.** Results of the tsunami source inversion. (a) Spatial distribution of the tsunami source.
 282 Contour lines denote the subsided region with intervals of 20 cm. The white star is the JMA
 283 epicenter, and blue triangles denote the location of the seafloor survey, where fresh surface
 284 cracks were found. The yellow and gray circles show the S-net OBPB locations used or not used,
 285 respectively, for inversion analysis. Comparisons of (b) the pressure waveforms and (c) the time-
 286 derivative waveforms. The gray and red traces denote the observed waveforms and simulated
 287 waveforms from the tsunami source model. Traces marked by blue lines denote the time window
 288 used for the inversion analysis.
 289



290

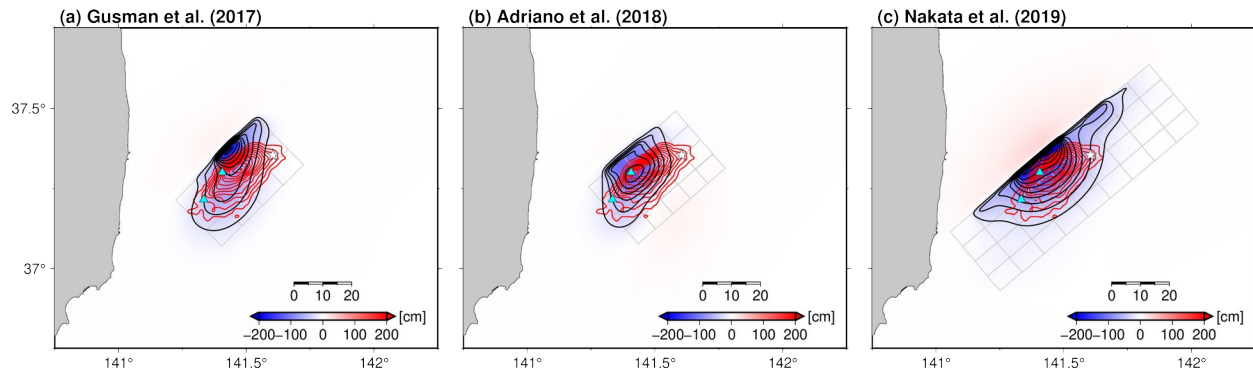
291 **Figure 5.** Waveform comparisons for the other tsunami stations, from the tsunami source model,
 292 for (a) NOWPHAS Near-coastal GPS buoys, (b) NOWPHAS wave gauges, (c) OBPGs installed
 293 by ERI, and (d) OBPGs installed by Tohoku University. At station 801, the waveforms during
 294 the data missing are not drawn. See Figure 1 for station locations.

295

296 In the inversion, we used the time-derivative waveforms of the pressure to reduce the
297 artificials attributed to the tsunami-irrelevant pressure components (Kubota, Suzuki et al., 2018).
298 In order to see how well this method reduced the artificials, we also conduct the additional
299 inversion using the original pressure waveforms, instead of its time-derivative waveforms
300 (Figure S2). The weight of the smoothing is also determined based on the VR between the
301 observed and simulated pressure waveforms (Figure S1). As a result, the distribution of the
302 tsunami source is fundamentally similar to the original distribution, although a significant
303 artificial uplift of > 60 cm is estimated around S2N14 where the large step was recorded. In order
304 to avoid this artificial due to the tsunami-irrelevant components, using the inversion method by
305 time-derivative waveforms (Kubota, Suzuki et al., 2018) worked very well to reduce the artificial
306 due to the apparent step signals irrelevant to the tsunami or the seafloor displacement.

307 We compare the tsunami source model estimated by the present study with the models
308 obtained using the tsunami data, except for the S-net data, by Gusman et al. (2017) (Figure 6a),
309 Adriano et al. (2018) (Figure 6b), and Nakata et al. (2019) (Figure 6c). The horizontal location
310 and spatial extent of the subsided region of our tsunami source model roughly correspond to
311 those obtained by the previous studies. However, the amount of the maximum subsidence was
312 much larger than the previous models and the locations of the peak subsidence of tsunami source
313 are slightly different from each other. Our tsunami source model had a maximum subsidence of
314 ~ 238 cm, whereas the two models obtained from the far-field tsunami data (Gusman et al. 2017;
315 Adriano et al., 2018) underestimated the subsidence (~ 180 cm and ~ 130 cm, respectively, Table
316 1). The subsidence peak of our model was located ~ 5 – 10 km southeast of the models by Gusman
317 et al. (2017) and Nakata et al. (2019) and ~ 10 km east of the model by Adriano et al. (2018). One
318 reason for these differences may be the assumption of the fault geometry, but the more
319 significant reason should be the station coverage and the source-station distance. The coastal tide
320 gauges or the offshore stations used in these previous studies were located far from the source
321 region and the stations at the offshore side of the source region were not used in these studies,
322 whereas the S-net has better station coverage and a smaller source-station distance. This could
323 provide a better constraint on the horizontal location and peak displacement amount to reproduce
324 surprisingly well the tsunami waveforms not used for the inversion. Thanks to this improvement
325 in the constraint, we believe that we can obtain a finite fault model with a higher resolution, as
326 shown in the next section.

327



328

329 **Figure 6.** Comparison of the tsunami source calculated from the finite fault models of the
 330 previous studies (black contours) and the tsunami source model (red). Models of (a) Gusman et
 331 al. (2017), (b) Adriano et al. (2018), and (c) Nakata et al. (2019) are shown. The contour
 332 intervals are 20 cm. The configuration of the fault is also shown by gray lines.

333

334 5 Fault modeling

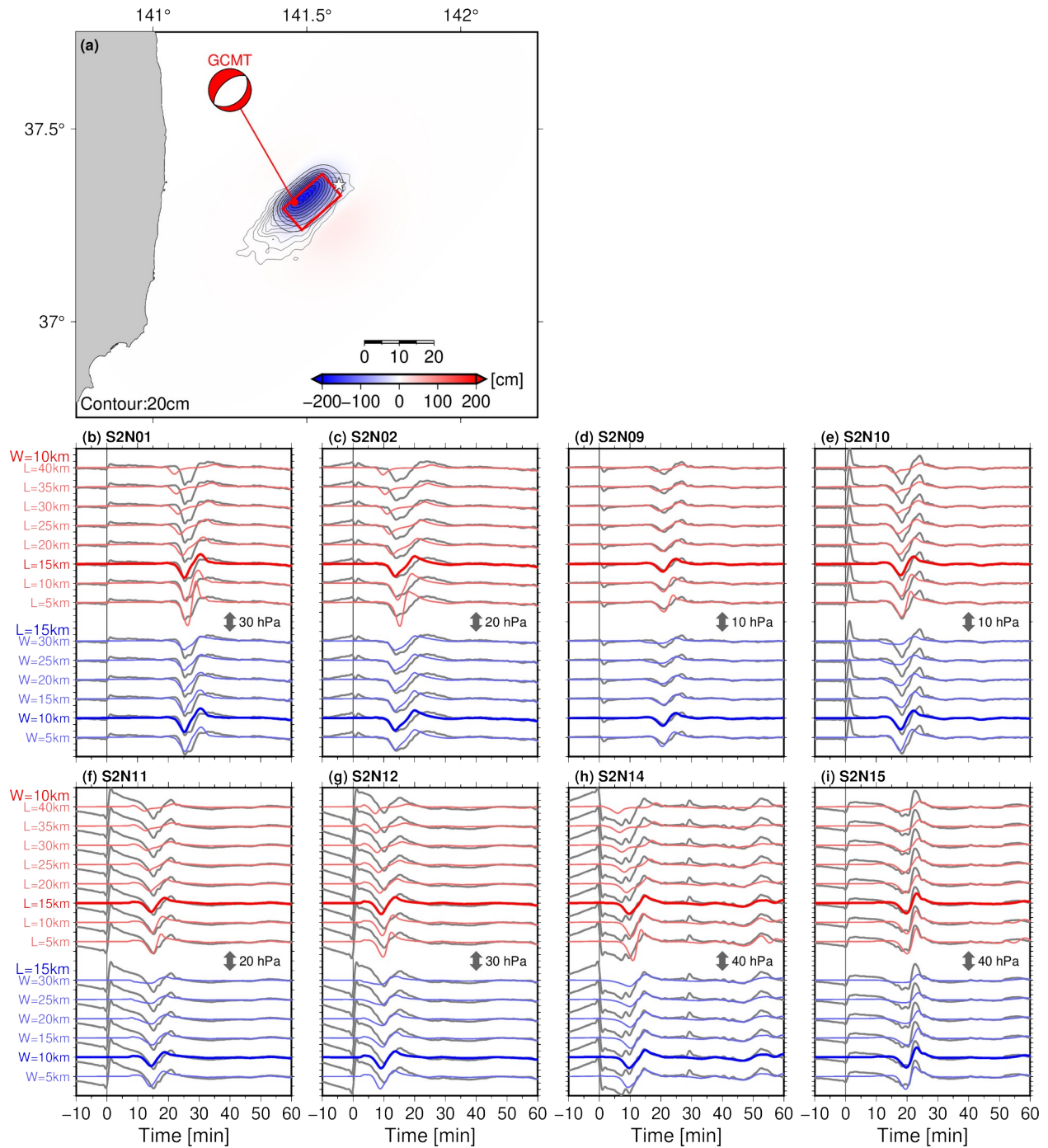
335 5.1 Rectangular fault model with uniform slip

336 Here, we attempt to constrain the finite fault model of the off-Fukushima earthquake.
 337 The horizontal location and the peak subsidence of our tsunami source distribution are slightly
 338 different from the other previous models. Therefore, we first constrained the optimum fault
 339 location based on a grid-search approach (Kubota et al., 2015; 2019). In the grid-search, we
 340 assume one planar rectangular fault with a uniform slip. The strike angle of the fault is fixed to
 341 the GCMT value (strike = 49°), considering the consistency with the direction of the northeast-
 342 southwest extent of the tsunami source. Since the dip and rake angles cannot be constrained only
 343 from the tsunami source, we assume these angles based on the GCMT solution (dip = 35° and
 344 rake = -89°), as inferred from the analysis of the teleseismic data. To find the optimum model
 345 that best reproduces the S-net waveforms, we vary the other fault parameters and simulate
 346 tsunamis. The unknown parameters of the rectangular fault that we search are the fault center
 347 location (longitude, latitude, and depth) and its dimensions (length L and width W). The slip
 348 amount on fault D is adjusted to maximize the VR in Eq. (4). The search range for these
 349 parameters is summarized in Table S1, which is determined based on the tsunami source model
 350 obtained in the previous section. Using an assumed rectangular fault with a set of parameters (the

351 fault model candidate), we calculated the seafloor displacement (Okada, 1992) and simulated the
352 tsunamis. The goodness of each of the fault model candidates is evaluated using the VR values.

353 The horizontal location of the optimum fault is shown in Figure 7a. The detailed
354 results of the grid-search analysis are shown in Figure S3. We obtain the optimum fault model as
355 $L = 15$ km, $W = 10$ km, and $D = 467.7$ cm ($M_0 = 2.1 \times 10^{19}$ Nm, M_w 6.8, assuming a rigidity of μ
356 $= 30$ GPa). The center of this model is located at a depth of 10 km, ~ 10 km east of the GCMT
357 centroid (the detailed parameters are listed in Table 1). The GCMT centroid depth was 12 km
358 and the aftershocks are mainly located at depths of ~ 20 km (Figures 1b and 1c), whereas the
359 estimated fault is located at the very shallow part of the crust (Figure 1c and Table 1). This
360 disagreement has also been pointed out by Gusman et al. (2017) from their numerical
361 simulations. They suggested that the aftershocks determined from the inland network are
362 systematically deeper than the actual depth. The horizontal extent of the tsunami source is
363 relatively narrow and is located at the northeast, compared with that obtained by the inversion
364 analysis (Figures 7a and S3a). The reproductivity of the S-net pressure waveforms is reasonable
365 (Figures S3b and S3c), although the VR is lower than that for the tsunami source inversion
366 ($VR_{\text{optimum}} = 59.3\%$). These mismatches are probably because of the simple assumption of the
367 rectangular fault, which could not reproduce the southwest part of the tsunami source.

368



369

370 **Figure 7.** (a) Horizontal location of the optimum rectangular fault model. The red rectangle

371 shows the location of the rectangular fault model. (b–i) Evaluation of the fault dimension.

372 Comparisons of the stations near the epicenter between the observed (gray) waveform and the

373 simulated waveforms from the varied fault dimensions are shown. The simulated waveforms

374 with thick red and blue traces denote the optimum rectangular fault.

375

376 If we consider the empirical scaling relations from the magnitude, then the fault
377 dimension is expected to be $\sim 700 \text{ km}^2$ (e.g., Wells & Coppersmith, 1994). On the other hand, the
378 estimated fault dimension of 150 km^2 is much smaller. In order to assess the dimensions of the
379 rectangular fault, we simulate tsunamis, fixing the seismic moment M_0 and the fault center
380 location to the optimum model and varying the fault dimensions. In Figures 7b to 7i, we compare
381 the waveforms of representative S-net stations relatively close to the focal area. If we assume a
382 larger fault with $L > 20 \text{ km}$, then the arrival of the peak downheaval wave and its amplitude
383 cannot be explained for the stations located northward (S2N01 and S2N02) or southward (S2N14
384 and S2N15) from the source. In addition, the sharp peak of the downheaval waves observed at
385 the stations located eastward (S2N09, S2N10, S2N11, S2N12, and S2N15) from the source are
386 not well reproduced by the fault width for the case in which $W > 15 \text{ km}$. These results suggest
387 that the fault dimensions should be $L \leq \sim 20 \text{ km}$ and $W \leq \sim 15 \text{ km}$. Considering this range, the
388 estimated fault dimensions are obviously smaller than expected based on the scaling relation.
389 These much smaller fault dimensions are consistent with the size of the asperity, defined as the
390 region of the large slip on the fault (e.g., Somerville et al., 1999), expected from the empirical
391 relation deduced from the inland crustal earthquakes (Somerville et al., 1999; Miyakoshi et al.,
392 2020). This may suggest that this optimum rectangular fault corresponds to the asperity.

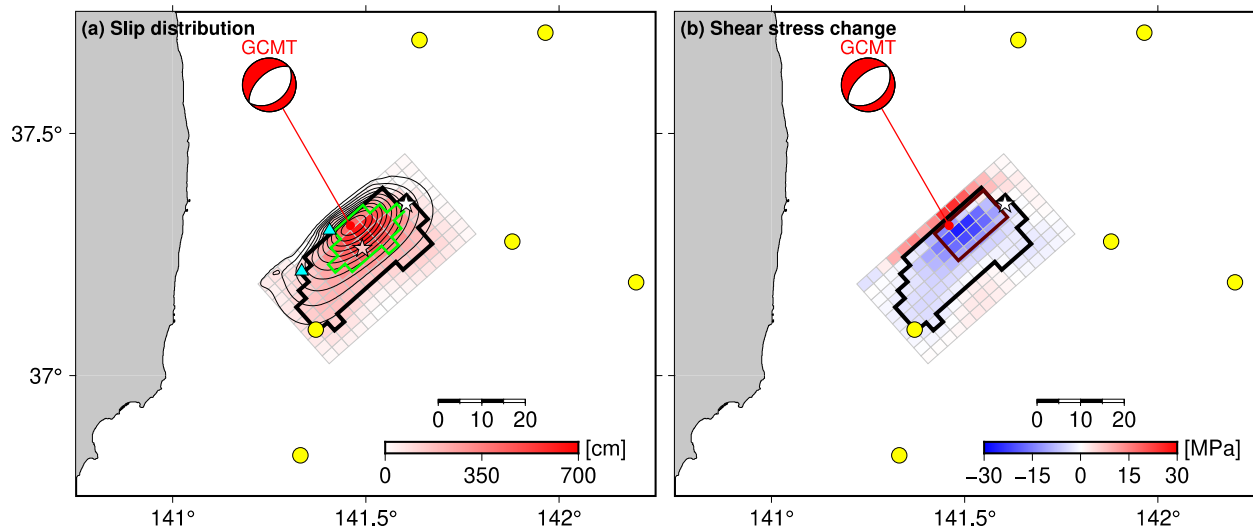
393

394 5.2 Slip distribution

395 We then conduct a finite fault inversion to estimate the slip distribution (finite fault
396 model) in a similar manner to that reported by Kubota, Saito et al. (2018). We assume a
397 rectangular planar fault with dimensions of $45 \text{ km} \times 30 \text{ km}$, so that the fault passes through the
398 optimum fault obtained by the grid search. The planar fault is divided into subfaults with size 3
399 $\text{ km} \times 3 \text{ km}$. We then simulate the Green's function, i.e., the pressure change waveforms excited
400 by each subfault, using a similar calculation procedure to that used in the grid-search analysis.
401 The inversion scheme is almost the same as the tsunami source inversion analysis, but we
402 imposed a nonnegativity constraint (Lawson & Hanson, 1974). The weighting of the smoothing
403 constraint is determined by trial and error.

404 The slip distribution obtained by the inversion analysis and the tsunami source
405 distribution calculated from this slip distribution are shown in is shown in Figure 8a. The
406 tsunami source distribution is similar to that obtained by the tsunami source inversion (Figure 4).

407 The S-net and other tsunamis waveforms are well explained ($VR = 72.4\%$, Figures S4b, S4c, and
 408 S5). We obtain a maximum slip of $D_{\max} = 637.2$ cm, and the total seismic moment is $M_0 = 6.3 \times$
 409 10^{19} Nm ($M_w 7.1$, $\mu = 30$ GPa). The large slip is concentrated in the northeastern part of the fault
 410 plane, corresponding to the rectangular fault estimated by the grid-search analysis. More
 411 specifically, subfaults with slip amounts with $D > 0.5 \times D_{\max}$ roughly correspond to the
 412 rectangular fault (subfaults marked by green lines in Figure 8a, 41% of the total M_0 , $M_w 6.9$). In
 413 addition, a relatively small slip also extends to the southwestern part, which was not resolved in
 414 the grid-search analysis. The reason why this slip was not resolved in the grid search is probably
 415 the simple assumption of the uniform slip rectangular fault. If we take subfaults with slip
 416 amounts larger than $0.2 \times D_{\max}$, then both large northeastern slip and relatively small
 417 southwestern slip are included (indicated by the thick black lines in Figure 8). Thus, we define
 418 these subfaults as the rupture area. The rupture area had dimensions of ~ 30 km \times ~ 20 km, and
 419 81% of the total moment was concentrated in the main rupture area. The horizontal location of
 420 the centroid, defined as the slip-weighted average of subfaults within the rupture area (pink star
 421 in Figure 8a, Table 1), is located ~ 5 km southeast from the GCMT centroid.
 422



423
 424 **Figure 8.** Result of the slip inversion. (a) Slip distribution (colored tiles) and tsunami source
 425 distribution (black contours, 20 cm interval). The pink and white stars indicate the slip-weighted
 426 averaged centroid and the JMA epicenter, respectively. Subfaults with slip amounts larger than
 427 $0.2 \times D_{\max}$ and larger than $0.5 \times D_{\max}$ are marked by thick black lines and green lines,
 428 respectively. (b) Shear stress change along the fault. Negative (blue) and positive (red) denote

429 the shear stress decrease and increase, respectively. The dark red rectangle denotes the optimum
 430 rectangular fault obtained by the grid-search analysis.

431

432 In Figure 8b, we calculate the distribution of the shear stress change along the fault,
 433 using the equation of Okada (1992). The rectangular fault estimated by the grid-search analysis
 434 agrees well with the region where the shear stress is largely released (green rectangle in Figure
 435 8b), indicating that the rectangular fault model corresponds to the asperity, as discussed above.
 436 Using the shear stress change distribution, we calculate the energy-based stress drop $\Delta\sigma_E$ (Noda
 437 et al., 2013) as:

438

$$439 \quad \Delta\sigma_E = \frac{\sum_i^{\square} D_i \Delta\sigma_i}{\sum_i^{\square} D_i}, \quad (7)$$

440

441 where D_i is the slip amount at the i -th subfault, and $\Delta\sigma_i$ is the stress drop at the i -th fault, which is
 442 defined as the shear stress change (Figure 8b) multiplied by -1 . Using the subfaults within the
 443 rupture area, we obtain $\Delta\sigma_E = 10.0$ MPa. This stress drop seems not so small as expected for the
 444 interplate earthquakes (an order of $\sim 10^0$ MPa, e.g., Kanamori & Anderson 1975), but rather is
 445 consistent with the intraplate earthquakes, which generally have stress drop values of $\sim 10^1$ MPa
 446 (e.g., Somerville et al., 1999; Miyakoshi et al., 2020).

447

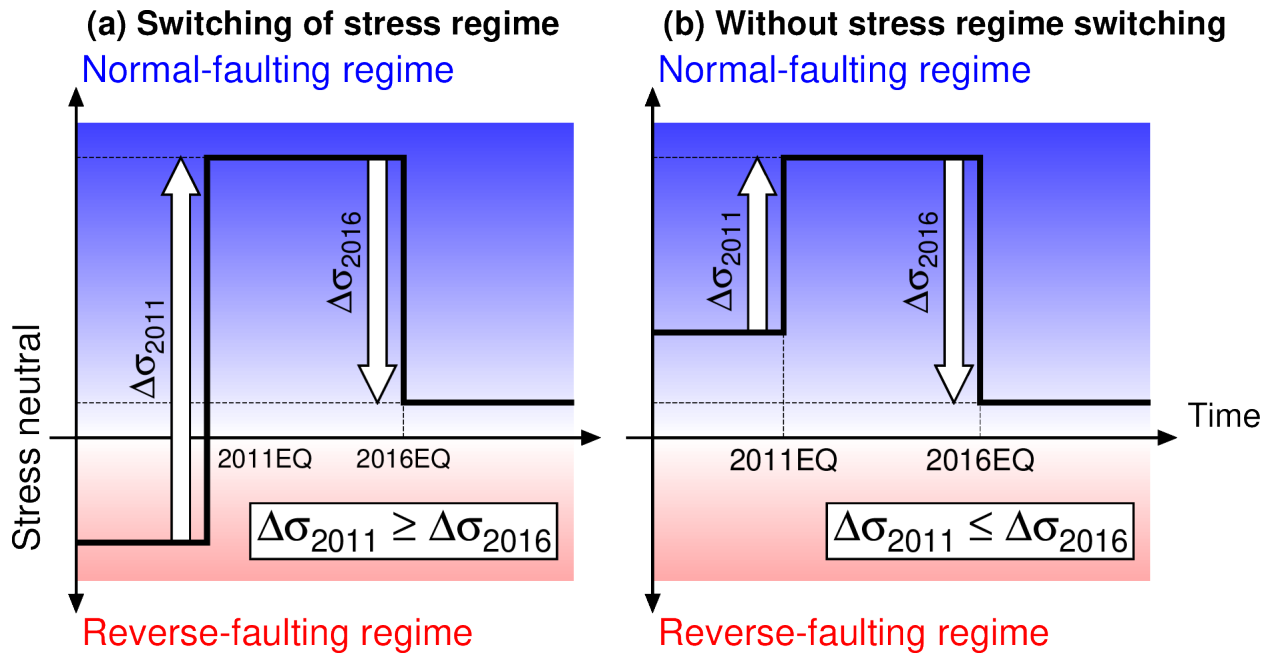
448 **6. Discussion: implication for the intraplate stress regime**

449 After the 2011 Tohoku earthquake, it has been reported that the normal-faulting
 450 seismicity significantly increased in the upper plate, which is thought to be related to the stress
 451 perturbation by the Tohoku earthquake (Figures 1d–1f, Asano et al., 2011; Hasegawa et al.,
 452 2012; Yoshida et al., 2012). The 2016 off-Fukushima earthquake is also considered to be an
 453 event of the normal-faulting seismicity related to the stress perturbation by the Tohoku
 454 earthquake. This change in seismicity is interpreted as the result whereby the intraplate stress
 455 regime switched after the Tohoku earthquake from the horizontal compression to the horizontal
 456 extension (e.g., Hasegawa et al. 2012). As discussed previously, the use of the S-net tsunami data

457 improved the constraint on the tsunami source and the fault model of the off-Fukushima
458 earthquake, which made it possible to obtain the detailed distribution of the shear stress
459 reduction and the static stress drop. Using these results, we attempt to discuss the quantitative
460 relationship between the crustal stress released during the off-Fukushima earthquake and the
461 stress increase due to the 2011 Tohoku earthquake. This kind of discussion is typically difficult
462 to conduct because it is rare that both the high-resolution fault model of the M~7 offshore
463 earthquake and the significant stress perturbation due to the megathrust earthquake are available.

464 If the stress regime switched by the Tohoku earthquake in the vicinity of the off-
465 Fukushima earthquake, the deviatoric stress, or the initial shear stress on the fault of the off-
466 Fukushima earthquake, should be smaller than (or at least equivalent to) the static shear stress
467 increase due to the Tohoku earthquake (Figure 9a). In other words, the stress drop of the off-
468 Fukushima earthquake should be smaller than the shear stress increase due to the Tohoku
469 earthquake. In Figure 10a, we calculate the shear stress change due to the Tohoku earthquake,
470 using the fault model of Iinuma et al. (2012), along the fault geometry of the off-Fukushima
471 earthquake. The shear stress change related to the Tohoku earthquake around the focal area of
472 the off-Fukushima earthquake is only ~2 MPa, which is smaller than the stress drop of the off-
473 Fukushima earthquake. The larger stress drop of the off-Fukushima earthquake than the stress
474 increase after the Tohoku earthquake is inconsistent with the presumption that the intraplate
475 stress regime switched by the static stress change of the Tohoku earthquake. There should be
476 other causes for the normal-faulting stress regime around the focal area of the off-Fukushima
477 earthquake.

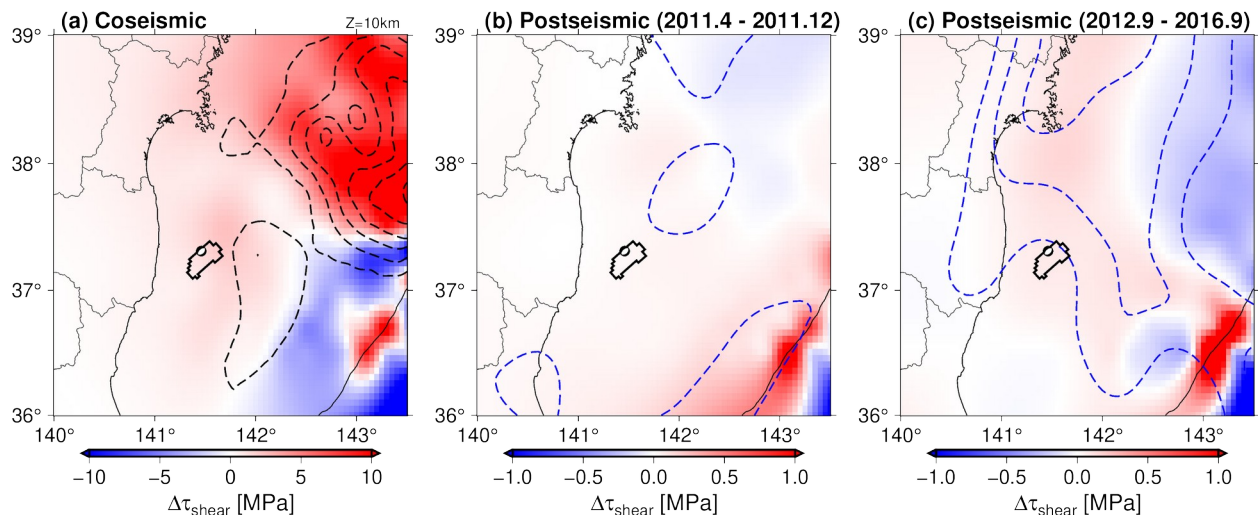
478



479

480 **Figure 9.** Schematic illustration of the temporal change of the stress regime around the off-
 481 Fukushima earthquake. The stress regimes (a) assuming the switching of the stress regime after
 482 the Tohoku earthquake and (b) without assuming the stress switching.

483



484

485 **Figure 10.** Horizontal distribution of the shear stress change on the 2016 off-Fukushima
 486 earthquake fault at a depth of 10 km. Shear stress changes along the fault geometry of the off-
 487 Fukushima earthquake due to (a) the Tohoku earthquake (Iinuma et al. 2012), (b) postseismic
 488 slip during April 2011 and December 2011 (Iinuma et al., 2016), and (c) Postseismic slip during
 489 September 2012 and September 2016 (Tomita et al. 2020). The main rupture area of the 2016

490 off-Fukushima earthquake inferred from the inversion analysis is also indicated by black lines.
491 Note that the color scales are different in each subfigure.

492

493 One possible cause is the postseismic slip of the Tohoku earthquake (Iinuma et al.,
494 2016; Tomita et al., 2020). After the Tohoku earthquake, the postseismic seafloor deformation
495 was detected by the seafloor geodetic observation (Tomita et al., 2015; 2017), which was caused
496 by the postseismic slip along the fault and the viscoelastic deformation (Sun et al., 2014; Iinuma
497 et al., 2016; Tomita et al., 2020). Among the postseismic deformation, the afterslip along the
498 plate interface is dominant in the south of the rupture area of the Tohoku earthquake, including
499 the region off Fukushima, whereas the viscoelastic deformation dominates the northern part of
500 the Tohoku earthquake rupture area (Iinuma et al., 2016; Tomita et al., 2020). Therefore, we
501 calculate the shear stress change on the 2016 fault geometry using the postseismic slip models to
502 evaluate the contribution by the postseismic slip around the focal area. We calculate the stress
503 change using the postseismic slip model from 23 April 2011 to 10 December 2011 proposed by
504 Iinuma et al. (2016) (Figure 10b). The calculated shear stress change is too small (on the order of
505 10^{-1} hPa) to complement the shortage of the stress change of the off-Fukushima earthquake. We
506 also calculated the stress change using the postseismic slip model during 2012 and 2016 (Tomita
507 et al., 2020) and found that its contribution was also minor (Figure 10c). We therefore concluded
508 that the shear stress increase due to the postseismic slip could not resolve the apparent
509 contradiction between the stress drop of the off-Fukushima earthquake and the shear stress
510 increase after the Tohoku earthquake. This contradiction arose from the assumption of the
511 switching of the stress regime, which was a reverse-faulting and a normal-faulting regime before
512 and after the Tohoku earthquake, respectively.

513 It was thought that the horizontal compressive stress attributed to the plate coupling
514 force was widely dominant in Japan before the Tohoku earthquake (e.g., Wang & Suyehiro,
515 1999; Terakawa & Matsu'ura, 2010). However, there are some recent reports that some normal-
516 faulting microearthquakes occurred even before the Tohoku earthquake in the inland region of
517 Fukushima prefecture (Imanishi et al., 2012; Yoshida et al., 2015a; 2015b). This normal-faulting
518 seismicity was interpreted as a result of the normal-faulting stress regime being predominant in
519 this location even before the Tohoku earthquake. One possible reason for this normal-faulting
520 stress regime is the effect of bending of the overriding plate, in which the horizontal extensional

521 and compressional stresses develop at the shallower and the deeper portion of the plate,
522 respectively (e.g., Turcotte & Schubert, 2002; Hashimoto & Matsu'ura 2006; Fukahata &
523 Matsu'ura, 2016). Yoshida et al. (2015a) showed that the normal-faulting stress regime is
524 dominant at depths shallower than ~ 15 km in this region, while the reverse-faulting stress regime
525 is dominant at depths greater than ~ 15 km, which is consistent with the hypothesis. We can also
526 consider the topographic effects (Wang et al., 2019) for the formation of the horizontal
527 extensional stress. Taking these past studies into account, it is reasonable to interpret this
528 apparent contradiction, in which the stress perturbation by the Tohoku earthquake around the off-
529 Fukushima earthquake is insufficient to switch the intraplate stress regime, that the horizontal
530 extensional stress regime was already predominant around the 2016 off-Fukushima earthquake
531 even before the Tohoku earthquake (Figure 9b).

532 Some major normal-faulting earthquakes were reported around the focal area of the
533 off-Fukushima earthquake in 1938 (Abe, 1977; Murotani, 2018). Furthermore, according to the
534 geologic cross-section around the off-Iwaki gas field, which is located near the 2016 off-
535 Fukushima earthquake, the northeast-southwest-trending reverse faults were developed at a
536 depth shallower than 6 km, which are considered to have formed during Oligocene and Miocene
537 (Iwata et al., 2002). Along this fault trace, it was also reported that the normal-faulting-type
538 surface offsets with vertical offset of 5–10 m were found, and it was suggested that the direction
539 of the tectonic stress flipped to the normal-faulting regime during Quaternary and a normal-
540 faulting earthquake similar to the 2016 off-Fukushima earthquake repeatedly occurred along this
541 fault (S. Toda, [https://irides.tohoku.ac.jp/media/files/earthquake/eq/2016_fukushima_eq/
542 20161122_fukushima_eq_activefault_toda.pdf](https://irides.tohoku.ac.jp/media/files/earthquake/eq/2016_fukushima_eq/20161122_fukushima_eq_activefault_toda.pdf), in Japanese). These reports may support our
543 hypothesis that the crustal stress regime was under the normal-faulting regime even before the
544 Tohoku earthquake.

545 Note that the downdip limit of the main rupture area of our fault model the off-
546 Fukushima earthquake is ~ 14 km, which is approximately consistent with the downdip limit
547 depth of the normal-faulting regime in the inland Fukushima region estimated by Yoshida et al.
548 (2015a). This suggests that the horizontal extensional stress regime before the Tohoku
549 earthquake around the focal area of the off-Fukushima earthquake is predominant at depths
550 shallower than 15 km and the stress neutral zone related to bending of the overriding plate lies at
551 a depth of ~ 15 km. We also note that the normal-faulting seismicity extensively increased in the

552 overriding plate, even at a depth deeper than 15 km (e.g., Asano et al., 2011; Hasegawa et al.,
553 2012). This might suggest that the stress-neutral depth was slightly deepened around this region
554 after the Tohoku earthquake.

555 As a summary of this discussion, the temporal change of the intraplate crustal stress
556 around the off-Fukushima earthquake can be interpreted as follows. The horizontal extensional
557 stress was predominant before the Tohoku earthquake within the shallowest part of the
558 continental plate, but may not exceed the crustal strength. After the Tohoku earthquake, its stress
559 perturbation enhanced the extensional stress, provoking the normal-faulting seismicity.

560 Before the 2011 Tohoku earthquake, no major seismicity was detected around the focal
561 area of the off-Fukushima earthquake (e.g., Asano et al., 2011; Hasegawa et al., 2012) and the
562 onshore seismic network could not detect micro-seismicity around this offshore region. On the
563 other hand, the use of the S-net OBPGs could well constrain the fault modeling of the 2016 off-
564 Fukushima earthquake, which provides an important implication for the crustal stress regime
565 prior to the Tohoku earthquake, even though the S-net was not installed at that time. Such
566 information about the stress regime is important to understand the spatio-temporal change of the
567 intraplate stress state and the generation mechanisms of the intraplate earthquake, especially after
568 a large megathrust earthquake. Our analysis demonstrated that the analysis of the offshore S-net
569 data provided implications for the crustal stress regime at the offshore region, which was
570 difficult to discuss before the S-net was available. Although the S-net OBPG data contains the
571 tsunami-irrelevant pressure change signals, careful analysis of this data significantly improves
572 the constraint of the fault model and will deepen our understanding of the earthquake generation.
573

574 **7 Conclusions**

575 We examined the S-net tsunami data associated with the off-Fukushima earthquake on
576 21 November 2016 (M_w 7.1). We first processed the S-net OBPG data and found some pressure
577 signals irrelevant to tsunami were observed: (1) an extremely large drift component and (2) an
578 abrupt pressure step around the origin time. We discussed the cause of these tsunami-irrelevant
579 signals and concluded that these signals were not due to the pressure sensors themselves but
580 probably due to the observation system. We then analyzed the S-net data in order to estimate the
581 tsunami source model and the fault model. Careful analysis of the S-net OBPG data provided the
582 tsunami source distribution, which had a large subsidence with strike angle consistent with the

583 GCMT solution. Our fault model suggested that the energy-based stress drop of the off-
584 Fukushima earthquake is $\Delta\sigma_E \sim 10$ MPa. The quantitative comparison between the stress drop and
585 the static stress changes caused by the 2011 Tohoku earthquake and its postseismic slip
586 suggested that the additional source of the horizontal extensional stress is necessary to explain
587 the stress drop. We interpreted the stress regime around the off-Fukushima earthquake to be the
588 horizontal extensional even before the Tohoku earthquake, related to the bending of the
589 overriding plate. The S-net pressure data is very useful to constrain the tsunami source model
590 and the finite fault model, even if the model is perturbed by the tsunami-irrelevant signals, which
591 provided an important implication for the tectonic stress regime within the overriding plate.

592

593 **Data Availability Statement**

594 The S-net OBPG data are available from the website of the National Research Institute
595 for Earth Science and Disaster Resilience [NIED] (NIED, 2019,
596 <https://doi.org/10.17598/NIED.0007>). The NOWPHAS tsunami data is provided upon request to
597 the Port and Airport Research Institute (PARI). The data of the OBPGs installed by ERI was
598 provided upon request to ERI, the University of Tokyo. The OBPG data of Tohoku University
599 was provided upon request to Ryota Hino of Tohoku University. Station locations of the S-net
600 OBPG are available at https://www.seafloor.bosai.go.jp/st_info/. The location of the OBPGs
601 installed by the ERI is available in Gusman et al. (2017). The locations of the NOWPHAS GPS
602 buoys and wave gauges are available at <https://nowphas.mlit.go.jp/pastdata/>. The locations of the
603 OBPGs installed by Tohoku University are listed in Table S2.

604 We purchased the JTOPO30v2 bathymetry data from the Marine Information
605 Research Center (<http://www.mirc.jha.jp/en/>) of the Japan Hydrographic Association. The plate
606 boundary model in Figure 1 (Nakajima & Hasegawa, 2006) is available from the website of
607 Fuyuki Hirose (<https://www.mri-jma.go.jp/Dep/sei/fhirose/plate/PlateData.html>, in Japanese,
608 accessed on 1 April, 2021). The rotation data of the S-net sensor (Takagi et al., 2019) was
609 provided by Ryota Takagi. The slip models of the mainshock and postseismic slip of Iinuma et
610 al. (2012; 2016) and Tomita et al. (2020) were provided by Takeshi Iinuma and Fumiaki Tomita.
611 The slip distribution models of Gusman et al. (2017), Adriano et al. (2018), and Nakata et al.
612 (2019) are available in each paper. The location of the seafloor bathymetry survey conducted by
613 the Japan Agency for Marine-Earth Science and Technology [JAMSTEC] (blue triangles in

614 Figure 4a) was taken from <http://www.jamstec.go.jp/ceat/j/topics/20161208.html>,
615 http://www.jamstec.go.jp/j/about/press_release/20170301/ (in Japanese).

616

617 **Acknowledgments**

618 The present study was supported by JSPS KAKENHI Grant Number JP19K14818 and
619 JP19H02409 from the Japan Society for the Promotion of Science. Discussions with Ryota Hino,
620 Naoki Uchida, and Tatsuhiko Saito, about interpreting the S-net pressure signals and the results
621 of the fault modeling, were fruitful. We would also like to thank Ryota Takagi, Takeshi Iinuma,
622 and Fumiaki Tomita for providing their useful data.

623

624 **References**

- 625 Abe, K. (1977). Tectonic implications of the large shioya-oki earthquakes of 1938. *Tectonophys*,
626 *41*, 269–289. [https://doi.org/10.1016/0040-1951\(77\)90136-6](https://doi.org/10.1016/0040-1951(77)90136-6)
- 627 Adriano, B., Fujii, Y., & Koshimura, S. (2018). Tsunami source and inundation features around
628 Sendai Coast, Japan, due to the November 22, 2016 Mw 6.9 Fukushima earthquake.
629 *Geoscience Letters*, *5*, 2. <https://doi.org/10.1186/s40562-017-0100-9>
- 630 Aoi, S., Suzuki, W., Chikasada, N. Y., Miyoshi, T., Arikawa, T., & Seki, K. (2019).
631 Development and utilization of real-time tsunami inundation forecast system using s-
632 net data. *Journal of Disaster Research*, *14*(2), 212–224.
633 <https://doi.org/10.20965/jdr.2019.p0212>
- 634 Aoi, S., Asano, Y., Kunugi, T., Kimura, T., Uehira, K., Takahashi, N., & Ueda, H. (2020).
635 MOWLAS : NIED observation network for earthquake , tsunami and volcano. *Earth*,
636 *Planets and Space*, *72*, 126. <https://doi.org/10.1186/s40623-020-01250-x>
- 637 Asano, Y., Saito, T., Ito, Y., Shiomi, K., Hirose, H., Matsumoto, T., ... Sekiguchi, S. (2011).
638 Spatial distribution and focal mechanisms of aftershocks of the 2011 off the Pacific
639 coast of Tohoku Earthquake. *Earth, Planets and Space*, *63*, 669–673. <https://doi.org/10.5047/eps.2011.06.016>
- 640
- 641 Baba, T., Hirata, K., Hori, T., & Sakaguchi, H. (2006). Offshore geodetic data conducive to the
642 estimation of the afterslip distribution following the 2003 Tokachi-oki earthquake.
643 *Earth and Planetary Science Letters*, *241*, 281–292.
644 <https://doi.org/10.1016/j.epsl.2005.10.019>
- 645 Chadwick, W. W. J., Nooner, S. L., Zumberge, M. A., Embley, R. W., & Fox, C. G. (2006).
646 Vertical deformation monitoring at Axial Seamount since its 1998 eruption using
647 deep-sea pressure sensors. *Journal of Volcanology and Geothermal Research*, *150*,
648 313–327. <https://doi.org/10.1016/j.jvolgeores.2005.07.006>
- 649 Fukahata, Y., & Matsu'ura, M. (2016). Deformation of island-arc lithosphere due to steady plate
650 subduction. *Geophysical Journal International*, *204*, 825–840.
651 <https://doi.org/10.1093/gji/ggv482>
- 652 Fukuyama, E., Ishida, M., Dreger, D. S., & Kawai, H. (1998). Automated seismic moment tensor
653 determination by using on-line broadband seismic waveforms. *Zisin 2*, *51*, 149–156
654 (in Japanese with English abstract). https://doi.org/10.4294/zisin1948.51.1_149

- 655 Gusman, A. R., Satake, K., Shinohara, M., Sakai, S., & Tanioka, Y. (2017). Fault slip
656 distribution of the 2016 Fukushima earthquake estimated from tsunami waveforms.
657 *Pure and Applied Geophysics*, *174*, 2925–2943. [https://doi.org/10.1007/s00024-017-](https://doi.org/10.1007/s00024-017-1590-2)
658 1590-2
- 659 Hardebeck, J. L., & Okada, T. (2018). Temporal stress changes caused by earthquakes: a review.
660 *Journal of Geophysical Research: Solid Earth*, *123*, 1350–1365.
661 <https://doi.org/10.1002/2017JB014617>
- 662 Hasegawa, A., Yoshida, K., Asano, Y., Okada, T., Iinuma, T., & Ito, Y. (2012). Change in stress
663 field after the 2011 great Tohoku-Oki earthquake. *Earth and Planetary Science*
664 *Letters*, *355–356*, 231–243. <https://doi.org/10.1016/j.epsl.2012.08.042>
- 665 Hashimoto, C., & Matsu'ura, M. (2006). 3-D simulation of tectonic loading at convergent plate
666 boundary zones: Internal stress fields in northeast Japan. *Pure and Applied*
667 *Geophysics*, *163(9)*, 1803–1817. <https://doi.org/10.1007/s00024-006-0098-y>
- 668 Hino, R. (2015). An overview of the Mw 9, 11 March 2011, Tohoku earthquake. *Summary of the*
669 *Bulletin of the International Seismological Centre*, *48*, 100–132.
670 <https://doi.org/10.5281/zenodo.998789>
- 671 Hino, R.? (2021) Ocean bottom pressure gauge data during the 2016 Fukushima-Oki earthquake
672 installed by Tohoku University [Data set]. Zenodo.
673 <http://doi.org/10.5281/zenodo.xxxxxxx>
- 674 Hino, R., Inazu, D., Ohta, Y., Ito, Y., Suzuki, S., Iinuma, T., ... Kaneda, Y. (2014). Was the
675 2011 Tohoku-Oki earthquake preceded by aseismic preslip? Examination of seafloor
676 vertical deformation data near the epicenter. *Marine Geophysical Research*, *35*, 181–
677 190. <https://doi.org/10.1007/s11001-013-9208-2>
- 678 Hua, Y., Zhao, D., Toyokuni, G., & Xu, Y. (2020). Tomography of the source zone of the great
679 2011 Tohoku earthquake. *Nature Communications*, *11*, 1163. [https://doi.org/10.1038/](https://doi.org/10.1038/s41467-020-14745-8)
680 s41467-020-14745-8
- 681 Iinuma, T., Hino, R., Kido, M., Inazu, D., Osada, Y., Ito, Y., ... Miura, S. (2012). Coseismic slip
682 distribution of the 2011 off the Pacific Coast of Tohoku Earthquake (M9.0) refined
683 by means of seafloor geodetic data. *Journal of Geophysical Research*, *117*, B07409.
684 <https://doi.org/10.1029/2012JB009186>

- 685 Iinuma, T., Hino, R., Uchida, N., Nakamura, W., Kido, M., Osada, Y., & Miura, S. (2016).
686 Seafloor observations indicate spatial separation of coseismic and postseismic slips
687 in the 2011 Tohoku earthquake. *Nature Communications*, 7, 13506.
688 <https://doi.org/10.1038/ncomms13506>
- 689 Imanishi, K., Ando, R., & Kuwahara, Y. (2012). Unusual shallow normal-faulting earthquake
690 sequence in compressional northeast Japan activated after the 2011 off the Pacific
691 coast of Tohoku earthquake. *Geophysical Research Letters*, 39(9), L09306.
692 <https://doi.org/10.1029/2012GL051491>
- 693 Inazu, D., & Hino, R. (2011). Temperature correction and usefulness of ocean bottom pressure
694 data from cabled seafloor observatories around Japan for analyses of tsunamis, ocean
695 tides, and low-frequency geophysical phenomena. *Earth, Planets and Space*, 63(11),
696 1133–1149. <https://doi.org/10.5047/eps.2011.07.014>
- 697 Inoue, M., Tanioka, Y., & Yamanaka, Y. (2019). Method for near-real time estimation of
698 Tsunami sources using ocean bottom pressure sensor network (S-net). *Geosciences*,
699 9, 310. <https://doi.org/10.3390/geosciences9070310>
- 700 Iwata, T., Hirai, A., Inaba, T., & Hirano, M. (2002). Petroleum system in the Offshore Joban
701 Basin, northeast Japan. *Journal of the Japanese Association for Petroleum*
702 *Technology*, 67(1), 62–71 (in Japanese with English abstract).
703 https://doi.org/10.3720/japt.67.1_62
- 704 Kanamori, H., & Anderson, D. L. (1975). Theoretical basis of some empirical relations in
705 seismology. *Bulletin of the Seismological Society of America*, 65(5), 1073–1095.
- 706 Kanazawa, T., & Hasegawa, A. (1997). Ocean-bottom observatory for earthquakes and tsunami
707 off Sanriku, north-eastern Japan using submarine cable. *Proceedings of International*
708 *Workshop on Scientific Use of Submarine Cables*, 208–209.
- 709 Kanazawa, T., Uehira, K., Mochizuki, M., Shinbo, T., Fujimoto, H., Noguchi, S., et al. (2016).
710 *S-net project, cabled observation network for earthquake and tsunamis* [Conference
711 presentation]. Suboptic2016, Dubai.
712 [https://suboptic.org/wp-content/uploads/fromke-vin/program/WE2B.3%20S-net](https://suboptic.org/wp-content/uploads/fromke-vin/program/WE2B.3%20S-net%20Project,%20Cabled%20Observation%20Network%20for%20Earthquakes%20and%20Tsunamis.pdf)
713 [%20Project,%20Cabled%20Observation%20Network%20for%20Earthquakes](https://suboptic.org/wp-content/uploads/fromke-vin/program/WE2B.3%20S-net%20Project,%20Cabled%20Observation%20Network%20for%20Earthquakes%20and%20Tsunamis.pdf)
714 [%20and%20Tsunamis.pdf](https://suboptic.org/wp-content/uploads/fromke-vin/program/WE2B.3%20S-net%20Project,%20Cabled%20Observation%20Network%20for%20Earthquakes%20and%20Tsunamis.pdf)

- 715 Kawaguchi, K., Sakuraba, S., Nagai, T., Nakai, K., Nukada, K., & Murase, H. (2017).
716 Characteristics of observed low frequency wave profiles of the 2016 Fukushima-Off
717 earthquake at offshore, shallow sea and coastal stations. *Journal of Japan Society of*
718 *Civil Engineers, Ser. B3 (Ocean Engineering)*, 73(2), I_743-I_748.
719 https://doi.org/10.2208/jscejoe.73.I_743
- 720 Kodaira, S., Fujiwara, T., Fujie, G., Nakamura, Y., & Kanamatsu, T. (2020). Large coseismic
721 slip to the trench during the 2011 Tohoku-Oki earthquake. *Annual Review of Earth*
722 *and Planetary Sciences*, 48, 321–343. [https://doi.org/10.1146/annurev-earth-071719-](https://doi.org/10.1146/annurev-earth-071719-055216)
723 [055216](https://doi.org/10.1146/annurev-earth-071719-055216)
- 724 Kodaira, S., Iinuma, T., & Imai, K. (2021). Investigating a tsunamigenic megathrust earthquake
725 in the Japan Trench. *Science*, 371, eabe1169. <https://doi.org/10.1126/science.abe1169>
- 726 Kubota, T., Hino, R., Inazu, D., Ito, Y., & Iinuma, T. (2015). Complicated rupture process of the
727 Mw 7.0 intraslab strike-slip earthquake in the Tohoku region on 10 July 2011
728 revealed by near-field pressure records. *Geophysical Research Letters*, 42, 9733–
729 9739. <https://doi.org/10.1002/2015GL066101>
- 730 Kubota, T., Suzuki, W., Nakamura, T., Chikasada, N. Y., Aoi, S., Takahashi, N., & Hino, R.
731 (2018). Tsunami source inversion using time-derivative waveform of offshore
732 pressure records to reduce effects of non-tsunami components. *Geophysical Journal*
733 *International*, 215, 1200–1214. <https://doi.org/10.1093/gji/ggy345>
- 734 Kubota, T., Saito, T., Ito, Y., Kaneko, Y., Wallace, L. M., Suzuki, S., Hino, R., & Henrys, S.
735 (2018). Using tsunami waves reflected at the coast to improve offshore earthquake
736 source parameters: application to the 2016 Mw 7.1 Te Araroa earthquake, New
737 Zealand. *Journal of Geophysical Research: Solid Earth*, 123, 8767–8779.
738 <https://doi.org/10.1029/2018JB015832>
- 739 Kubota, T., Saito, T., & Suzuki, W. (2020). Millimeter-scale tsunami detected by a wide and
740 dense observation array in the deep ocean: Fault modeling of an Mw 6.0 interplate
741 earthquake off Sanriku, NE Japan. *Geophysical Research Letters*, 47,
742 e2019GL085842. <https://doi.org/10.1029/2019GL085842>
- 743 Kubota, T., Saito, T., Chikasada, N. Y., & Suzuki, W. (2020). Ultrabroadband seismic and
744 tsunami wave observation of high-sampling ocean-bottom pressure gauge covering

- 745 periods from seconds to hours. *Earth and Space Science*, 7, e2020EA001197. <https://doi.org/10.1029/2020ea001197>
- 746
- 747 Kubota, T., Saito, T., Chikasada, N. Y., & Sandanbata, O. (2021). Meteotsunami observed by the
748 deep-ocean seafloor pressure gauge network off northeastern Japan. [Preprint]. *Earth
749 and Space Science Open Archive*. <https://doi.org/10.1002/essoar.10506159.1>
- 750 Lay, T. (2018). A review of the rupture characteristics of the 2011 Tohoku-oki Mw 9.1
751 earthquake. *Tectonophysics*, 733, 4–36. <https://doi.org/10.1016/j.tecto.2017.09.022>
- 752 Matsubara, M., Sato, H., Uehira, K., Mochizuki, M., Kanazawa, T., Takahashi, N., Suzuki, K., &
753 Kamiya, S. (2019). Seismic velocity structure in and around the Japanese Island arc
754 derived from seismic tomography including NIED MOWLAS Hi-net and S-net data.
755 In M. Kanao & G. Toyokuni (Eds.), *Seismic Waves - Probing Earth System*.
756 IntechOpen. <https://doi.org/10.5772/intechopen.86936>.
- 757 Matsumoto, K., Takanezawa, T., & Ooe, M. (2000). Ocean tide models developed by
758 assimilating TOPEX/POSEIDON altimeter data into hydrodynamical model: A
759 global model and a regional model around Japan. *Journal of Oceanography*, 56,
760 567–581. <https://doi.org/10.1023/A:1011157212596>
- 761 Miyakoshi, K., Somei, K., Yoshida, K., Kurahashi, S., Irikura, K., & Kamae, K. (2020). Scaling
762 Relationships of Source Parameters of Inland Crustal Earthquakes in Tectonically
763 Active Regions. *Pure and Applied Geophysics*, 177, 1917–1929.
764 <https://doi.org/10.1007/s00024-019-02160-0>
- 765 Mochizuki, M., Kanazawa, T., Uehira, K., Shimbo, T., Shiomi, K., Kunugi, T., et al. (2016). *S-
766 net project: Construction of large scale seafloor observatory network for tsunamis
767 and earthquakes in Japan* [Conference presentation]. AGU Fall Meeting 2016,
768 American Geophysical Union, San Francisco.
- 769 Mulia, I. E., & Satake, K. (2021). Synthetic analysis of the efficacy of the S-net system in
770 tsunami forecasting. *Earth, Planets and Space*, 73, 36.
771 <https://doi.org/10.1186/s40623-021-01368-6>
- 772 Murotani, S., Satake, K., & Fujii, Y. (2013). Scaling relations of seismic moment, rupture area,
773 average slip, and asperity size for M~9 subduction-zone earthquakes. *Geophysical
774 Research Letters*, 40, 5070–5074. <https://doi.org/10.1002/grl.50976>

- 775 Murotani, S. (2018) Natural disasters that reached a milestone in Fukushima –The 1888 eruption
776 of Bandai-san and the 1938 Fukushima-ken Toho-oki Earthquake– [Translated Title
777 from Japanese]. *Earthquake Journal*, 66, 30–39 (in Japanese). Retrieved January 16,
778 2021, from <https://www.adeq.or.jp/public/img/66.pdf>
- 779 Nagai, T. (1998). Development and improvement of the Japanese coastal wave observation
780 network (NOWPHAS). *Journal of Japan Society of Civil Engineers*, 609, 1–14.
781 https://doi.org/10.2208/jscej.1998.609_1
- 782 Nakajima, J., & Hasegawa, A. (2006). Anomalous low-velocity zone and linear alignment of
783 seismicity along it in the subducted Pacific slab beneath Kanto, Japan: Reactivation
784 of subducted fracture zone? *Geophysical Research Letters*, 33, L16309.
785 <https://doi.org/10.1029/2006GL026773>
- 786 Nakata, K., Hayashi, Y., Tsushima, H., Fujita, K., Yoshida, Y., & Katsumata, A. (2019).
787 Performance of uniform and heterogeneous slip distributions for the modeling of the
788 November 2016 off Fukushima earthquake and tsunami, Japan. *Earth, Planets and*
789 *Space*, 71(1), 30. <https://doi.org/10.1186/s40623-019-1010-1>
- 790 National Research Institute for Earth Science and Disaster Resilience [NIED] (2019). NIED S-
791 net [Data set]. <https://doi.org/10.17598/nied.0007>
- 792 Nishikawa, T., Matsuzawa, T., Ohta, K., Uchida, N., Nishimura, T., & Ide, S. (2019). The slow
793 earthquake spectrum in the Japan Trench illuminated by the S-net seafloor
794 observatories. *Science*, 365, 808–813. <https://doi.org/10.1126/science.aax5618>
- 795 Noda, H., Lapusta, N., & Kanamori, H. (2013). Comparison of average stress drop measures for
796 ruptures with heterogeneous stress change and implications for earthquake physics.
797 *Geophysical Journal International*, 193, 1691–1712.
798 <https://doi.org/10.1093/gji/ggt074>
- 799 Polster, A., Fabian, M., & Villinger, H. (2009). Effective resolution and drift of parascientific
800 pressure sensors derived from long-term seafloor measurements. *Geochemistry,*
801 *Geophysics, Geosystems*, 10(8), Q08008. <https://doi.org/10.1029/2009GC002532>
- 802 Saito, T. (2019). *Tsunami generation and propagation*. Springer Japan, Tokyo.
803 <https://doi.org/10.1007/978-4-431-56850-6>

- 804 Saito, T., Satake, K., & Furumura, T. (2010). Tsunami waveform inversion including dispersive
805 waves: The 2004 earthquake off Kii Peninsula, Japan. *Journal of Geophysical*
806 *Research*, *115*, B06303. <https://doi.org/10.1029/2009JB006884>
- 807 Saito, T., & Kubota, T. (2020). Tsunami modeling for the deep sea and inside focal areas.
808 *Annual Review of Earth and Planetary Sciences*, *48*, 121–145.
809 <https://doi.org/10.1146/annurev-earth-071719-054845>
- 810 Saito, T., Kubota, T., Chikasada, N. Y., Tanaka, Y., & Sandanbata, O. (2021). Meteorological
811 tsunami generation due to sea-surface pressure change: Three-dimensional theory
812 and synthetics of ocean-bottom pressure change [Preprint]. *Earth and Space Science*
813 *Open Archive*. <https://doi.org/10.1002/essoar.10504961.1>
- 814 Sawazaki, K., & Nakamura, T. (2020). “N”-shaped Y/X coda spectral ratio observed for in-line-
815 type OBS networks; S-net and ETMC: interpretation based on natural vibration of
816 pressure vessel. *Earth, Planets and Space*, *72*, 130. [https://doi.org/10.1186/s40623-](https://doi.org/10.1186/s40623-020-01255-6)
817 [020-01255-6](https://doi.org/10.1186/s40623-020-01255-6)
- 818 Somerville, P., Irikura, K., Graves, R., Sawada, S., Wald, D., Abrahamson, N., Iwasaki, Y.,
819 Kagawa, T., Smith, N., & Kowada, A. (1999). Characterizing crustal earthquake slip
820 models for the prediction of strong ground motion. *Seismological Research Letters*,
821 *70*, 59–80. <https://doi.org/10.1785/gssrl.70.1.59>
- 822 Sun, T., Wang, K., Iinuma, T., Hino, R., He, J., Fujimoto, H., ... Hu, Y. (2014). Prevalence of
823 viscoelastic relaxation after the 2011 Tohoku-oki earthquake. *Nature*, *514*(7520), 84–
824 87. <https://doi.org/10.1038/nature13778>
- 825 Suppasri, A., Leelawat, N., Latcharote, P., Roeber, V., Yamashita, K., Hayashi, A., ... Imamura,
826 F. (2017). The 2016 Fukushima earthquake and tsunami: Local tsunami behavior and
827 recommendations for tsunami disaster risk reduction. *International Journal of*
828 *Disaster Risk Reduction*, *21*, 323–330. <https://doi.org/10.1016/j.ijdr.2016.12.016>
- 829 Takagi, R., Uchida, N., Nakayama, T., Azuma, R., Ishigami, A., Okada, T., ... Shiomi, K.
830 (2019). Estimation of the orientations of the S-net cabled ocean-bottom sensors.
831 *Seismological Research Letters*, *90*, 2175–2187. <https://doi.org/10.1785/0220190093>
- 832 Takagi, R., Toyokuni, G., & Chikasada, N. (2020). Ambient noise correlation analysis of S-net
833 records: extracting surface wave signals below instrument noise levels. *Geophysical*
834 *Journal International*, *224*, 1640–1657. <https://doi.org/10.1093/gji/ggaa548>

- 835 Tanaka, M., Asano, K., Iwata, T., & Kubo, H. (2014). Source rupture process of the 2011
836 Fukushima-ken Hamadori earthquake: How did the two subparallel faults rupture?
837 *Earth, Planets and Space*, 66(1), 101. <https://doi.org/10.1186/1880-5981-66-101>
- 838 Tanaka, S., Matsuzawa, T., & Asano, Y. (2019). Shallow Low-Frequency Tremor in the
839 Northern Japan Trench Subduction Zone. *Geophysical Research Letters*, 46, 5217–
840 5224. <https://doi.org/10.1029/2019GL082817>
- 841 Tanioka, Y. (2020). Improvement of Near-field Tsunami Forecasting Method Using Ocean
842 Bottom Pressure Sensor Network (S-net). *Earth, Planets and Space*, 72, 132. <https://doi.org/10.1186/s40623-020-01268-1>
- 843
- 844 Terakawa, T., & Matsu'ura, M. (2010). The 3-D tectonic stress fields in and around Japan
845 inverted from centroid moment tensor data of seismic events. *Tectonics*, 29, TC6008.
846 <https://doi.org/10.1029/2009TC002626>
- 847 Toda, S., & Goto, H. (2016)
848 [https://irides.tohoku.ac.jp/media/files/earthquake/eq/2016_fukushima_eq/](https://irides.tohoku.ac.jp/media/files/earthquake/eq/2016_fukushima_eq/20161122_fukushima_eq_activefault_toda.pdf)
849 [20161122_fukushima_eq_activefault_toda.pdf](https://irides.tohoku.ac.jp/media/files/earthquake/eq/2016_fukushima_eq/20161122_fukushima_eq_activefault_toda.pdf)
- 850 Tomita, F., Kido, M., Osada, Y., Hino, R., Ohta, Y., & Iinuma, T. (2015). First measurement of
851 the displacement rate of the Pacific Plate near the Japan Trench after the 2011
852 Tohoku-Oki earthquake using GPS/acoustic technique. *Geophysical Research*
853 *Letters*, 42(20), 8391–8397. <https://doi.org/10.1002/2015GL065746>
- 854 Tomita, F., Kido, M., Ohta, Y., Iinuma, T., & Hino, R. (2017). Along-trench variation in seafloor
855 displacements after the 2011 Tohoku earthquake. *Science Advances*, 3, e1700113.
856 <https://doi.org/10.1126/sciadv.1700113>
- 857 Tomita, F., Iinuma, T., Ohta, Y., Hino, R., Kido, M., & Uchida, N. (2020). Improvement on
858 spatial resolution of a coseismic slip distribution using postseismic geodetic data
859 through a viscoelastic inversion. *Earth, Planets and Space*, 72, 84.
860 <https://doi.org/10.1186/s40623-020-01207-0>
- 861 Tsushima, H., Hino, R., Tanioka, Y., Imamura, F., & Fujimoto, H. (2012). Tsunami waveform
862 inversion incorporating permanent seafloor deformation and its application to
863 tsunami forecasting. *Journal of Geophysical Research*, 117, B03311. [https://doi.org/](https://doi.org/10.1029/2011JB008877)
864 [10.1029/2011JB008877](https://doi.org/10.1029/2011JB008877)

- 865 Tsushima, H., & Yamamoto, T. (2020). *Operational use of tsunami source inversion in near-*
 866 *field tsunami warning by JMA* [Conference presentation]. JpGU-AGU Joint Meeting
 867 2020 Virtual, Online. <https://confit.atlas.jp/guide/event/jpgu2020/subject/HDS08-12/>
 868 advanced
- 869 Uchida, N., Nakajima, J., Wang, K., Takagi, R., Yoshida, K., Nakayama, T., ... Asano, Y.
 870 (2020). Stagnant forearc mantle wedge inferred from mapping of shear-wave
 871 anisotropy using S-net seafloor seismometers. *Nature Communications*, *11*.
 872 <https://doi.org/10.1038/s41467-020-19541-y>
- 873 Uchida, N. & Burgmann, R. (2021). A Decade of Lessons Learned from the 2011 Tohoku-oki
 874 Earthquake [Preprint]. *Earth and Space Open Archive*.
 875 <https://doi.org/10.1002/essoar.10505694.1>
- 876 Uehira, K., Kanazawa, T., Mochizuki, M., Fujimoto, H., Noguchi, S., Shinbo, T., et al. (2016).
 877 *Outline of seafloor observation network for earthquakes and tsunamis along the*
 878 *Japan Trench (S-net)* [Conference presentation]. EGU General Assembly 2016,
 879 European Geosciences Union, Vienna, Austria.
- 880 Wallace, L. M., Araki, E., Saffer, D., Wang, X., Roesner, A., Kopf, A., ... Carr, S. (2016). Near-
 881 field observations of an offshore Mw 6.0 earthquake from an integrated seafloor and
 882 subseafloor monitoring network at the Nankai Trough, southwest Japan. *Journal of*
 883 *Geophysical Research: Solid Earth*, *121*, 8338–8351.
 884 <https://doi.org/10.1002/2016JB013417>
- 885 Wells, D. L., & Coppersmith, K. J. (1994). New empirical relationships among magnitude,
 886 rupture length, rupture width, rupture area, and surface displacement. *Bulletin of the*
 887 *Seismological Society of America*, *84*(4), 974–1002.
- 888 Wang, K., & Suyehiro, K. (1999). How does plate coupling affect crustal stresses in Northeast
 889 and Southwest Japan? *Geophysical Research Letters*, *26*(15), 2307–2310.
 890 <https://doi.org/10.1029/1999GL900528>
- 891 Wang, K., Sun, T., Brown, L., Hino, R., Tomita, F., Kido, M., ... Fujiwara, T. (2018). Learning
 892 from crustal deformation associated with the M9 2011 Tohoku-oki earthquake.
 893 *Geosphere*, *14*, 1–20. <https://doi.org/10.1130/GES01531.1>
- 894 Wang, K., Brown, L., Hu, Y., Yoshida, K., He, J., & Sun, T. (2019). Stable Forearc Stressed by a
 895 Weak Megathrust: Mechanical and Geodynamic Implications of Stress Changes

- 896 Caused by the M = 9 Tohoku-Oki Earthquake. *Journal of Geophysical Research:*
897 *Solid Earth*, 124, 6179–6194. <https://doi.org/10.1029/2018JB017043>
- 898 Wang, Y., & Satake, K. (2021). Real-time tsunami data assimilation of S-net pressure gauge
899 records during the 2016 Fukushima Earthquake. *Seismological Research Letters*.
900 <https://doi.org/10.1785/0220200447>
- 901 Watts, D. R., & Kontoyiannis, H. (1990). Deep-ocean bottom pressure measurement: drift
902 removal and performance. *Journal of Atmospheric and Oceanic Technology*, 7, 296–
903 306. [https://doi.org/10.1175/1520-0426\(1990\)007<0296:DOBPMD>2.0.CO;2](https://doi.org/10.1175/1520-0426(1990)007<0296:DOBPMD>2.0.CO;2)
- 904 Yamamoto, N., Aoi, S., Hirata, K., Suzuki, W., Kunugi, T., & Nakamura, H. (2016). Multi-index
905 method using offshore ocean-bottom pressure data for real-time tsunami forecast.
906 *Earth, Planets and Space*, 68, 128. <https://doi.org/10.1186/s40623-016-0500-7>
- 907 Yamamoto, N., Hirata, K., Aoi, S., Suzuki, W., Nakamura, H., & Kunugi, T. (2016). Rapid
908 estimation of tsunami source centroid location using a dense offshore observation
909 network. *Geophysical Research Letters*, 43, 4263–4269.
910 <https://doi.org/10.1002/2016GL068169>
- 911 Yoshida, K., Hasegawa, A., Okada, T., Iinuma, T., Ito, Y., & Asano, Y. (2012). Stress before and
912 after the 2011 great Tohoku-oki earthquake and induced earthquakes in inland areas
913 of eastern Japan. *Geophysical Research Letters*, 39(3), L03302.
914 <https://doi.org/10.1029/2011GL049729>
- 915 Yoshida, K., Hasegawa, A., & Okada, T. (2015a). Spatial variation of stress orientations in NE
916 Japan revealed by dense seismic observations. *Tectonophysics*, 647, 63–72.
917 <https://doi.org/10.1016/j.tecto.2015.02.013>
- 918 Yoshida, K., Hasegawa, A., & Okada, T. (2015b). Spatially heterogeneous stress field in the
919 source area of the 2011 Mw 6.6 Fukushima-Hamadori earthquake, NE Japan,
920 probably caused by static stress change. *Geophysical Journal International*, 201,
921 1062–1071. <https://doi.org/10.1093/gji/ggv068>
- 922 Yu, Z., & Zhao, D. (2020). Seismic evidence for water transportation in the forearc off northern
923 Japan. *Journal of Geophysical Research: Solid Earth*, 125, 2019JB018600.
924 <https://doi.org/10.1029/2019jb018600>
- 925
- 926

927

928 **Table 1.** Fault parameters for the rectangular fault models.

Models	Fault center location			M_0 [Nm]	Maximum vertical displacement [cm]	
	Longitude [°E]	Latitude [°N]	Depth [km] ^a		Uplift	Subsidence
GCMT solution	141.46	37.31	12.0	3.18×10^{19}	N/A	N/A
Tsunami source	N/A	N/A	N/A	N/A	16.3	238.4
Grid-search ^{ab}	141.5165	37.3105	6.0	2.10×10^{19}	16.0	193.1
Slip distribution ^a	141.4908 ^c	37.2630 ^c	7.7 ^c	6.30×10^{19}	10.5	237.4
Gusman et al. (2017)	N/A	N/A	N/A	3.70×10^{19}	10.1	182.6
Adriano et al. (2018)	N/A	N/A	N/A	3.35×10^{19}	8.5	130.6
Nakata et al. (2019)	N/A	N/A	N/A	8.52×10^{19}	29.7	222.2

929 ^aFault geometry is fixed to the GCMT value; strike = 49°, dip = 35°, rake = -89°.930 ^bFault dimension is $L = 15$ km, $W = 10$ km, and slip amount is $D = 467.7$ cm. The depths of the fault top and bottom are 3.1 km and 8.9
931 km, respectively.932 ^cSlip-weighted average location is shown.

933

934